J. Fluid Mech. (2008), *vol.* 600, *pp.* 45–76.
doi:10.1017/S0022112008000293 Printed in the United Kingdom

The cascade structure of linear instability in collapsible channel flows

X. Y. LUO[1], Z. X. CAI[2], W. G. LI[3] AND T. J. PEDLEY[4]

[1]Department of Mathematics, University of Glasgow, Glasgow Q12 8QW, UK
x.y.Luo@maths.gla.ac.uk

[2]Department of Mechanics, Tianjin University, China

[3]Department of Mechanical Engineering, University of Sheffield, Sheffield S1 3JD, UK

[4]Department of Applied Mathematics and Theoretical Physics, University of Cambridge, Wilberforce Road, Cambridge, CB3 0WA UK

(Received 13 November 2006 and in revised form 8 December 2007)

This paper studies the unsteady behaviour and linear stability of the flow in a collapsible channel using a fluid–beam model. The solid mechanics is analysed in a plane strain configuration, in which the principal stretch is defined with a zero initial strain. Two approaches are employed: unsteady numerical simulations solving the nonlinear fully coupled fluid–structure interaction problem; and the corresponding linearized eigenvalue approach solving the Orr–Sommerfeld equations modified by the beam. The two approaches give good agreement with each other in predicting the frequencies and growth rates of the perturbation modes, close to the neutral curves. For a given Reynolds number in the range of 200–600, a cascade of instabilities is discovered as the wall stiffness (or effective tension) is reduced. Under small perturbation to steady solutions for the same Reynolds number, the system loses stability by passing through a succession of unstable zones, with mode number increasing as the wall stiffness is decreased. It is found that this cascade structure can, in principle, be extended to many modes, depending on the parameters. A puzzling 'tongue' shaped stable zone in the wall stiffness–*Re* space turns out to be the zone sandwiched by the mode-2 and mode-3 instabilities. Self-excited oscillations dominated by modes 2–4 are found near their corresponding neutral curves. These modes can also interact and form period-doubling oscillations. Extensive comparisons of the results with existing analytical models are made, and a physical explanation for the cascade structure is proposed.

1. Introduction

Flow in collapsible tubes has been extensively studied in the last few decades. It is of interest in the fields of biomedical engineering and applied mathematics, both for its relevance to physiological applications and because of the dynamic behaviour of the system (Shapiro 1977; Jensen & Pedley 1989; Kamm & Pedley 1989; Luo & Pedley 1995, 1996, 1998, 2000; Matsuzaki & Fujimura 1995; Heil 1997; Paidoussis 1998, 2004; de Langre *et al.* 2007). Of particular interest are the mechanisms for the self-excited oscillations which are frequently observed in the laboratory in a 'Starling resistor', consisting of a length of elastic tube, mounted on two rigid tubes, contained in a pressurized chamber, and with a fluid flowing through the tube (e.g. Bertram 1982; Bertram, Raymond & Pedley 1990). Earlier works studied

such oscillations using one-dimensional models (e.g. Cancelli & Pedley 1985; Jensen 1990, 1992). In a one-dimensional model with constant longitudinal tension, Jensen (1990) showed that as downstream transmural pressure (internal minus external) is decreased for a given flow rate, the system first loses its stability to either mode-2 or mode-3 oscillations depending on the flow rate, and then to higher modes for decreased transmural pressure. (The mode number i, $i = 1, 2.3\ldots$, here means that the perturbation to the flexible segment contains i half-wavelengths.) In addition, he predicted mode interactions in which the system goes through a co-dimension 2, double-Hopf bifurcation.

Recent advances in numerical methods have made it possible to solve the nonlinear fluid–structure interactions fully, either in two dimensions (Luo & Pedley 1996, 1998, 2000; Pedley & Luo 1998; Cai & Luo 2003; Jensen & Heil 2003; Heil & Waters 2006), or in three dimensions (Hazel & Heil 2003; Jensen & Heil 2003; Marzo, Luo & Bertram 2005). Three-dimensional simulations will be required to provide direct comparisons with many of the dynamic phenomena observed in experiments (Bertram *et al.* 1990; Bertram & Elliott 2001). However, because of the huge computational resources they require, all the three-dimensional simulations so far have been limited to steady flows and have not yet succeeded in predicting the dynamical behaviour of the system. Two-dimensional approaches, on the other hand, can provide interesting flow details and maintain some key features of the three-dimensional systems, and are, in principle, realizable in the laboratory. Various self-excited oscillations have been revealed in a simple two-dimensional fluid–membrane model, in which a finite segment of one wall of a parallel-sided channel is replaced by a membrane under tension (Luo & Pedley 1996, 1998, 2000). The key feature of these studies is that the self-excited oscillations occur as a result of steady solutions becoming unstable to small-amplitude mode-2 perturbations, which then evolve via period-doubling and chaotic-like bifurcations to complex large-amplitude oscillations. Jensen & Heil (2003), using an asymptotic analysis and numerical simulations to study the system at large tension and high Reynolds number, were able to explain one physical mechanism for high-frequency self-excited oscillations. They showed that such oscillations grow by extracting kinetic energy from the mean Poiseuille flow faster than it is lost to viscous dissipation. However, this mechanism led only to mode-1 oscillations, and then only if the rigid channel downstream of the elastic segment was longer than the upstream channel. It is not clear whether the same mechanism can explain the mode-2 oscillations that frequently occur in the system with larger deformation (e.g. in the quoted papers by Luo & Pedley).

Stability of a plane channel flow between compliant walls has also been studied previously from a variety of points of view (Green & Ellen 1972; Webster *et al.* 1985; Carpenter & Garrad 1986; Grotberg & Gavriely 1989; Ehrenstein & Rossi 1993; Davies & Carpenter 1997*a*, *b*). Most of these studies considered the instability of flow in a long parallel-sided channel, so, in the basic state, the steady flow is unidirectional and the elastic walls are planar. Although these studies reveal various modes of instability (Tollmien–Schlichting waves, travelling-wave flutter, static divergence, and their interactions), they are difficult to apply to our finite-length non-parallel flow system. The steady flow in our problem, from which the oscillations grow, involves a large deformation of the wall and, usually, separation of the flow. Such a steady solution would be required as the basic state for a linear stability analysis.

In almost all of the two-dimensional models mentioned above, several *ad hoc* approximations are used to describe the elasticity of the solid wall. In particular, tangential displacement of the wall has usually been ignored, and the tension assumed

to be constant. Cai & Luo (2003) employed a new model in which the membrane is replaced by a plane-strained elastic beam with large deflection, and identified parameter regimes in which the constant tension assumption is valid, at least for steady flow. It is found that the steady behaviour of the beam model agrees well with the membrane (constant tension) model as long as the additional stretch-induced tension is small compared to the initial constant tension.

In this paper, the fluid–beam model is extended to study unsteady flows of the system. The stability of the system is studied systematically for zero initial tension. Two approaches are used. One is to solve the fully coupled unsteady Navier–Stokes equations and the nonlinear large displacement structural equations. In this approach, the ALE (arbitrary Lagrangian Eulerian) method combined with rotational spines is employed. The other is to solve the linear eigenvalue system of the Orr–Sommerfeld equation, modified by the beam, for perturbations to the nonlinear-large deformation steady solutions.

The eigenvalue approach has not been used in this context before, and the novel features of the full computations are the use of the rotational spine method for unsteady simulations, with zero initial tension, so that the solid mechanics of the wall is entirely rational, and a much enhanced mesh refinement. The eigenvalue approach enables us to identify precisely the linear onset of the self-excited oscillations, while the full computations allow us to follow the oscillations from their linear onset to the nonlinear large-amplitude stage. Using these approaches, we find that an intriguing 'tongue' appears in the neutral stability curve plotted on the effective tension–Reynolds number plane (the definition of the effective tension is given below). The presence of this 'tongue' means that, for a given Reynolds number, as the tension is lowered to a critical value, the system becomes unstable, which is to be expected. However, a further decrease of the tension re-stabilizes the system before it becomes unstable again (see figure 16 below).

In an effort to explain the physical mechanism underlying the 'tongue' phenomenon, we are able to demonstrate that the onset of the large-amplitude self-excited oscillations is indeed initiated by the linear instability of the system, and that the self-excited oscillations that develop when the system loses stability can consist of different modes. More importantly, we found that the 'tongue' is associated with a 'cascade' structure involving mode switching. In addition to mode-2, which has been reported in membrane papers, higher modes (modes 3 to 4) are also discovered. Based on this discovery, we offer a plausible physical explanation for the cascade structure in § 4.9.

2. The fluid–beam model

2.1. *Model description*

The model consists of a steady flow in a channel in which part of the upper wall is replaced by an elastic beam in the plane strain configuration (figure 1). The rigid channel has width D, a part of the upper wall of length L is replaced by a pre-stressed elastic beam subjected to an external pressure p_e. L_u and L_d are the lengths of the upstream and downstream rigid parts of the channel. Steady Poiseuille flow with average velocity U_0 is assumed at the entrance. The flow is incompressible and laminar, the fluid having density ρ and viscosity μ. The extensional and bending stiffnesses of the beam are EA and EJ, respectively, where E is the Young's modulus, A is the cross-sectional area of the beam (i.e. the beam's thickness, h, as the beam has unit width in the z-direction), and J is the moment of inertia of the beam cross-section. (As we consider a plane strain problem here, E is equivalent to the

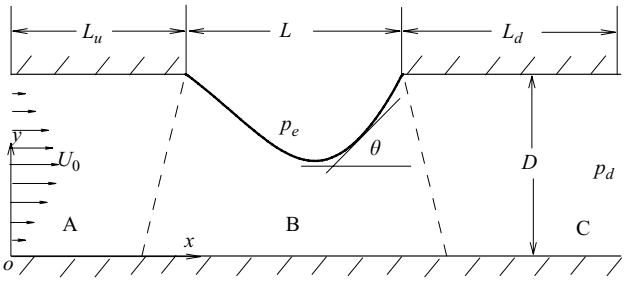

FIGURE 1. The flow-beam configuration (not to scale). In section B, part of the wall is replaced by an elastic beam.

conventional Young's modulus divided by (1-ν^2), where ν is the Poisson's ratio.) The pre-tension in the beam (caused by its initial stretch) is T and the density of the beam is ρ_m. Damping and rotational inertia of the beam are both neglected.

2.2. *The governing equations*

For convenience, the flow velocity components u_i, fluid stresses σ_{ij}, pressure p, time t, the Cartesian coordinates x, y (with origin at the left bottom of the channel), and length l are non-dimensionlized as follows:

$$\left.\begin{aligned} u_i^* = \frac{u_i}{U_0}, \quad \sigma_{ij}^* = \frac{\sigma_{ij}}{\rho U_0^2}, \quad p^* = \tfrac{p}{\rho U_0^2}, \quad t^* = \tfrac{tU_0}{D}, \quad l^* = \tfrac{l}{D}, \quad x^* = \tfrac{x}{D}, \\ y^* = \frac{y}{D} \quad (i, j = 1, 2), \end{aligned}\right\} \tag{1a}$$

and the non-dimensional parameters, such as the initial tension T, the curvature κ, the density of the beam ρ_m, the wall stiffnesses EA, EJ, and the Reynolds number are defined by

$$T^* = \frac{T}{\rho U_0^2 D}, \quad \kappa^* = \kappa D, \quad \rho_m^* = \frac{\rho_m h}{\rho D}, \quad c_\lambda = \frac{EA}{\rho U_0^2 D}, \quad c_\kappa = \frac{EJ}{\rho U_0^2 D^3}, \quad Re = \frac{U_0 D \rho}{\mu}. \tag{1b}$$

The starred variables are non-dimensional, a convention which will be used throughout this paper. In the following, however, the stars are dropped for simplicity.

The governing equations for the fluid flow are the Navier–Stokes equations

$$\frac{\partial u_i}{\partial t} + u_j u_{i,j} = -p_{,i} + \frac{1}{Re} u_{i,jj} \quad (i, j = 1, 2), \tag{2}$$

$$u_{i,i} = 0 \qquad (i, j = 1, 2). \tag{3}$$

By employing the Kirchhoff constitutive laws for the elastic beam, we can write the following dimensionless governing equations for the beam (for derivation of these equations see Cai & Luo 2003):

$$\frac{\rho_m}{\lambda}\left(x'\frac{\mathrm{d}^2 x}{\mathrm{d}t^2} + y'\frac{\mathrm{d}^2 y}{\mathrm{d}t^2}\right) = c_\kappa \kappa \kappa' + c_\lambda \lambda' + \lambda \tau_n, \tag{4}$$

$$\frac{\rho_m}{\lambda}\left(y'\frac{\mathrm{d}^2 x}{\mathrm{d}t^2} - x'\frac{\mathrm{d}^2 y}{\mathrm{d}t^2}\right) = c_\kappa \left(\frac{1}{\lambda}\kappa'\right)' - \lambda \kappa T - c_\lambda \lambda \kappa (\lambda - 1) - \lambda \sigma_n + \lambda p_e, \tag{5}$$

$$x' = \lambda \cos\theta, \quad y' = \lambda \sin\theta, \quad \theta' = \lambda \kappa, \tag{6}$$

where the superscript prime represents a derivative with respect to the longitudinal coordinate in the beam in the horizontal position, l. Also $\lambda = \sqrt{x'^2 + y'^2}$ is the

principal stretch of the beam, θ is the rotation angle of the beam relative to the x-axis as shown in figure 1, and σ_n and τ_n are the normal and shear stresses exerted by the fluid on the beam:

$$\sigma_n = p - \frac{2}{Re}\frac{\partial u_n}{\partial n}, \tau_n = -\frac{1}{Re}\left(\frac{\partial u_s}{\partial n} + \frac{\partial u_n}{\partial s}\right), \tag{7}$$

where s and n indicate the tangential and the normal direction of the beam. Note that as both c_κ and $c_\lambda \to 0$, we recover the fluid–membrane model. Throughout this study, we choose $c_\kappa/c_\lambda = (h^2/12D^2) \approx 10^{-5}$ (for a beam thickness of about 1% of the channel height). Effects of different wall thickness on the steady flows have been studied elsewhere (Marzo *et al.* 2005; Luo *et al.* 2007).

Boundary conditions for the flow field are chosen such that there is a steady parabolic velocity profile at the upstream inlet, the stress-free condition is used for the downstream outlet, and the no-slip condition is used along the walls including the elastic section. Clamped conditions are used for the two ends of the beam. A constant external pressure p_e is applied outside the elastic wall. In this paper, the non-dimensional external pressure is taken to be $p_e = 1.95$.

3. Methods

3.1. *Fully coupled finite-element equations*

A finite-element code for unsteady flow is used to solve the coupled nonlinear fluid–structure interactive equations simultaneously, and an adaptive mesh with rotating spines is used to allow for the movable boundary. The mesh is divided into three subdomains, A, B and C (figure 1). The subdomain B is the section with the elastic wall, and is covered with many spines originating from the bottom rigid wall to material points in the movable beam.

These spines are straight lines, which can rotate around the fixed nodes at the bottom. All finite-element nodes in subdomain B are associated with their specific spines. Thus all the nodes on the spines can be stretched or compressed depending on the beam deformation.

A Petrov–Galerkin method is used to discretize the system equations (2)–(6). The element type for flow is six-node triangular with second-order shape function N_i for u and v, and linear shape function L_i for p. Three-node beam elements with second-order shape function are used for x, y, θ, λ and κ. The discretized finite-element equations can be written in a matrix form as

$$\boldsymbol{M}(\boldsymbol{U})\frac{\mathrm{d}\boldsymbol{U}}{\mathrm{d}t} + \boldsymbol{K}(\boldsymbol{U})\boldsymbol{U} - \boldsymbol{F} \equiv R = 0, \tag{8}$$

where $\boldsymbol{U} = (u_j, v_j, p_j, x_j, y_j, \theta_j, \lambda_j, \kappa_j)$ is the global vector of unknowns, and $j = 1, \ldots, n$, is the nodal number. $\boldsymbol{R}$ is the overall residual vector which is denoted by

$$\boldsymbol{R} = (R_x, R_y, R_c, R_{ex}, R_{ey}, R_{e\theta}, R_{e\lambda}, R_{e\kappa}), \tag{9}$$

where the subscripts x, y, c indicate the corresponding residuals of the $x-$ and y-momentum and continuity equations in the fluid (equations (2)–(3)), and $e_x, e_y, e_\theta, e_\lambda, e_\kappa$ indicate the corresponding residuals of equations (4)–(6).

3.2. *The unsteady solutions and initial conditions*

An implicit finite-difference second-order predictor–corrector scheme with a variable time step is used to solve the time-dependent problem. At each time step, the frontal

method and a Newton–Raphson scheme are employed to obtain the converged solution for the whole system simultaneously. For details, see Luo & Pedley (1996).

Before we study the unsteady behaviour of the system, a steady solution is obtained. This is done by solving (8) with $\mathrm{d}\boldsymbol{U}/\mathrm{d}t = 0$ for a given set of parameters, as was done by Cai & Luo (2003). Then, in order to test the solution stability, a small perturbation is applied to the steady solution and the time evolution is computed. This is done by using a slightly different steady solution as the initial guess, which has a parameter value of c_λ, say, that is 1% away from that of the steady solution in question. If the unsteady solution converges to the corresponding steady solution, then the solution is considered to be stable. If, as time progresses, the unsteady solution diverges away from the steady solution or oscillates with time, then it is deemed to be unstable. The critical point at which the system becomes unstable is called the neutrally stable point.

3.3. *The eigensolver*

As our numerical perturbations to the steady solutions are not strictly infinitesimal, it is not evident that the small-amplitude oscillations definitely correspond to linear instability of the system. To investigate this, we solve the eigenvalue problem of the linearized finite-element equations, which is essentially the discretized Orr–Sommerfeld eigenvalue system, modified by the elastic beam.

We denote the infinitesimal perturbation to a steady solution $\bar{U}$ by ΔU, so that $U = \bar{U} + \Delta U$ is a solution to the system. Here, $\bar{U}$ is obtained from a full numerical simulation as described in § 3.1. If the system is stable, then U approaches $\bar{U}$ as time increases. Writing ΔU in the form of $\mathrm{e}^{\omega t}\tilde{\boldsymbol{U}}$, where $\omega\,(= \omega_r + \mathrm{i}\omega_i)$, $\tilde{\boldsymbol{U}}$ are the complex eigenvalue and eigenvector, respectively, and substituting into (8), we obtain a matrix eigenvalue equation:

$$(\omega\bar{\boldsymbol{M}} + \bar{\boldsymbol{K}})\tilde{\boldsymbol{U}} \equiv \tilde{\boldsymbol{R}} = 0, \tag{10}$$

where the matrices $\bar{\boldsymbol{M}}$, $\bar{\boldsymbol{K}}$ are determined by the steady solution $\bar{\boldsymbol{U}}$. The matrix equation (10) is solved by using a QZ algorithm (Garbow 1978), which solves for the complete set of eigensolutions of the system.

The QZ algorithm is extremely inefficient for solving the large-matrix complex-eigenvalue problem as it solves for the complete set of eigensolutions of the discretized system. When the grid is fine, this means over ten thousand eigensolutions are solved for, which is not the most efficient way of obtaining the leading few solutions. In this work, we also used a Muller solver (Barrodale & Wilson 1978), which is much faster and solves for one particular set of eigensolutions, and its results agree well with those of the QZ solver. However, this solver requires a close initial guess of the eigenfrequency, and therefore cannot be used from the start as we need to scan the parameter space for neutral stabilities.

3.4. *Numerical grids and accuracy*

Validations for the fully coupled Navier–Stokes solver have been performed extensively before for the steady case (Cai & Luo 2003), and the smallest viscous boundary-layer width is estimated to be about 0.014 for the parameters investigated. As the computations are extremely time-consuming, especially the complex QZ solver for the eigenvalue problem, a set of different grids is tested to achieve the required accuracy while ensuring that the computational cost is affordable. A grid that satisfies these criteria is one with $16 \times (30 + 60 + 60)$ elements with a stretch ratio of 1:10 towards the corners: this is used for the eigenvalue computations and steady-flow simulations. Full numerical results using this grid have been compared with those

obtained with a much finer mesh of $22 \times (70 + 120 + 200)$ elements, and the elastic wall deformations between the two are graphically indistinguishable. Most of the computations are performed on Euclid2, a twin Pentium 4 processors (3.4 GHz) Linux machine with 8GB memory at the University of Glasgow. The eigensolver requires about 14 CPU hours for each solution. For the full unsteady numerical simulations, since variable time steps are used, the temporal convergence of the time-dependent solutions is checked by using a different error tolerance ε between $\varepsilon = 10^{-3}$ and 10^{-6}. It was found that $\varepsilon = 10^{-5}$ is accurate enough for most of the oscillations (i.e. the time histories of the variables are almost graphically indistinguishable when $\varepsilon = 10^{-6}$ is used compared with $\varepsilon = 10^{-5}$). On Euclid2, the computations take about 0.1–1 CPU min for a typical steady solution or one time step of the unsteady solution.

4. Results

4.1. *Parameters and the definition of effective tension*

We choose the dimensional parameters to be: $\mu = 10^{-3}$ Pa s^{-1}, $\rho = 10^3$ kg m^{-3}, $D = 10^{-2}$ m, the dimensionless parameters as defined in § 2.2 are thus $L_u = 5$, $L = 5$, $L_d = 30$. In this particular study, we also focus on the parameter range with (dimensionless) $T = 0$, $\rho_m = 0$, $p_e = 1.95$, $Re = 1{-}600$ and $c_\lambda = 1{-}2500$. The values are chosen to be in the range of parameters that have been used extensively in previous studies with the membrane model (Luo & Pedley 1996, 2000) and the steady fluid–beam model (Cai & Luo 2003). In particular, T is chosen to be zero to ensure that the initial configuration is stress-free, and the values of ρ_m, p_e and c_λ are chosen because these were used when the strange 'tongue' was first identified for a non-zero tensioned beam (Luo & Cai 2004).

In order to compare our results with those of existing one- or two-dimensional models, we introduce the concept of the *effective tension*, which is the sum of the initial tension and the stretch-induced tension (assuming the contribution from the fluid shear stress is negligible):

$$T_e = T + c_\lambda(\lambda - 1). \tag{11}$$

Since the principal stretch λ varies along the beam, we can estimate the effective tension by calculating λ at a fixed station along the beam, e.g. the downstream end. This enables us to compare our results ($T = 0$) with earlier work (Luo & Cai 2004) where the initial tension was not zero, as well as with earlier models (Jensen 1990; Davies & Carpenter 1997*b*; Jensen & Heil, 2003) where the tension used was also the effective tension as the wall stretching was neglected.

In §§ 4.2–4.5, we first present results obtained using the eigensolver.

4.2. *The eigensolutions*

The eigensolutions, in terms of the maximum growth rate ω_r and the corresponding angular frequency ω_i, are plotted against Re for some fixed values of c_λ, as shown in Figure 2. It is seen that with the exception of $c_\lambda = 310$, all curves show some similar features. Both ω_r and ω_i increase with Re initially, and become flatter as Re increases. ω_r increases monotonically with Re for smaller values of c_λ ($= 500$, 1000) and, as Re is increased, ω_r crosses the x-axis to become positive. For these values of c_λ, the system is stable for smaller Re and unstable for higher Re. This is similar to what was observed for the membrane model (Luo & Pedley 1996). However, for greater values of c_λ ($c_\lambda = 1800$, 2400) the growth curve presents a peak: ω_r increases with Re at first, but decreases later on. The curve for $c_\lambda = 1800$ is particularly interesting, as

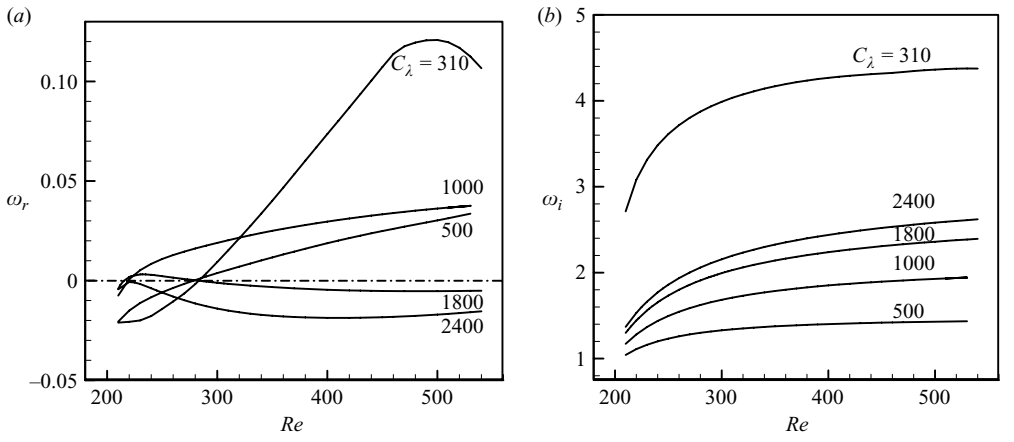

FIGURE 2. (a) The maximum growth rate ω_r and (*b*) the corresponding frequency ω_i, versus *Re* for $c_\lambda = 310$, 500, 1000, 1800 and 2400.

it crosses the x-axis twice. In this case, the system becomes unstable only for a small range of *Re* and is stable otherwise. For even greater values of c_λ (>2400), although the peak still exists, the curve is positioned entirely below the x-axis, so the system is stable for all *Re*.

The frequency (ω_i) variations with *Re* are more straightforward: they all increase as *Re* increases, and they are higher for greater value of c_λ (again, with the exception of $c_\lambda = 310$). This is as we might expect, as a stiffer wall oscillates at a higher frequency. The increase of frequency with *Re* is more rapid at the beginning; however, for *Re* greater than 300, the curves become flatter. This is qualitatively similar to the findings by Jensen & Heil (2003, figure 9), where they found that for high $Re(>300)$, the frequency is more or less independent of *Re*.

Note that the results for $c_\lambda = 310$ are markedly different from the rest of the curves: ω_r has a much larger peak and is positive for all $Re > 280$. Further analysis (in § 4.5) shows that all curves in figure 2, in fact, correspond to mode-2 disturbances, except the one with $c_\lambda = 310$, which corresponds to mode-3 disturbances.

4.3. *The neutral stability curve – a cascade structure*

The neutral stability curve consists of the set of all neutral points in the (c_λ, *Re*)-plane separating stable from unstable operating points, i.e. at which $\omega_r = 0$. This curve is obtained by solving for the eigensolution iteratively and scanning across a range of values of c_λ for each fixed value of *Re*. A bisection method is used to locate the neutral point. The neutral stability curve in the (c_λ, *Re*)-space is shown in figure 3. This figure reveals an interesting structure, with three distinct branches, marked as M-2, M-3 and M-4 (this notation is used because the different branches correspond to mode-2, mode-3 and mode-4 oscillations, as we shall see below). The system is stable on the left of the branches and above M-2, and is unstable on the right of the branches below M-2.

Initially, for a large value of $c_\lambda(>2270)$, the system is stable for all *Re* investigated. As c_λ is reduced, the system first loses its stability by crossing the upper branch M-2. However, as c_λ is further reduced (to the lower branch M-2), the system become re-stabilized before it becomes unstable again as a slightly lower value of c_λ (to the upper branch M-3). Further reduction of c_λ shows that the system can again be re-stabilized as the operating point crosses the small zone between the branches

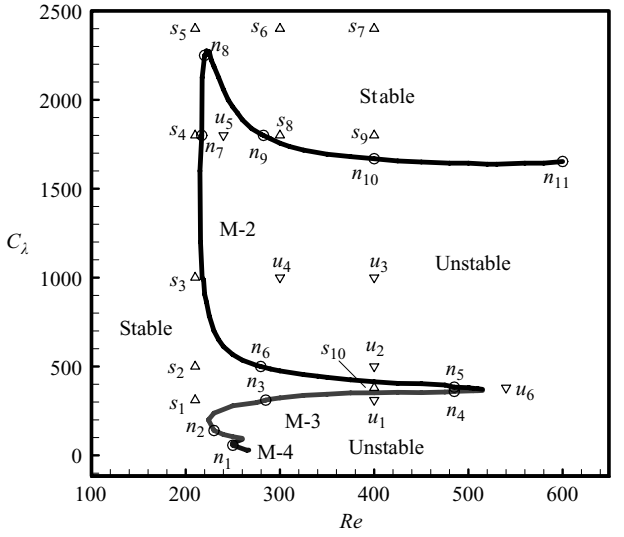

FIGURE 3. Neutral stability curve in the (c_λ, Re)-space. Branch M-2 goes through points n_5 to n_{11}, branch M-3 goes through n_2 to n_4, and branch M-4 goes through n_1. The system is stable on the left of the branches and the top of M-2, and on the right of branches (below M-2), it is unstable. Information of all the control points marked on the graph is given in table 1.

M-3 and M-4. These features are different from what was previously found for the membrane system, where the system is stable at higher values of the tension, and unstable when the tension falls below a critical value (Luo & Pedley 1996). We devote the rest of the paper to exploring and trying to explain these new features.

Figure 3 can be compared with the curves shown in figure 2. The point on the neutral curve of figure 3 at a particular value of c_λ is where the curve for that value of c_λ crosses the abscissa in figure 2(*a*). However, it is clearer in figure 3 that for only a small range of c_λ (between 1600 and 2270), are there two intersections. In other words, at these c_λ values, the system is unstable for only a small range of *Re*, but is stable otherwise. For values of c_λ between 10 and 1600, there is only one intersection. This means that there is one critical Reynolds number, above which the system is stable, and for $c_\lambda > 2270$, there is no intersection: the system is stable for all values of *Re* investigated.

To understand these results fully, we examine more closely a few selected operating points in the parameter space. These points are named n_i, s_i, u_i, where $i = 1, 2, 3, \ldots$, and n, s, u indicate that they are neutral, stable and unstable points, respectively (figure 3). Detailed information for these points is given in table 1.

4.4. *The neutral frequencies*

We now look at the corresponding neutral frequency, ω_i plotted against *Re* in figure 4. There are again three distinct branches, with branch M-2 having the lowest frequencies, and branch M-4 the highest, although there are some overlaps between branches M-3 and M-4. It is seen that the frequency on branches M-2 and M-3 is largely independent of *Re* for higher Reynolds numbers. However, it changes rapidly with *Re* for $Re < 300$. Branches M-3 and M-4 appear to be incomplete here. This is because we seek only the first neutral point encountered in the (Re, c_λ)-space (as *Re* is increased for fixed c_λ). Branch M-2 is the curve encountered first for most of the parameter range studied here, while branches M-3 and M-4 arise only when c_λ is

Zone	Point	Re	c_λ	ω_r eigensolver	ω_i eigensolver	ω_r (Levenberg–Marquardt)	ω_i (Levenberg–Marquardt)	ω_i (Fourier transform)	Unstable mode
Stable	s_1	210	310.94	-2.1087×10^{-2}	2.7117	-2.0987×10^{-2}	2.5821	0.9764, **2.6734**	Stable
	s_2	210	500	-2.0539×10^{-2}	1.0419	-1.9789×10^{-2}	1.0321	1.0354	Stable
	s_3	210	1000	-7.5000×10^{-3}	1.1709	-7.3621×10^{-3}	1.1563	1.1654	Stable
	s_4	210	1800	-4.0757×10^{-3}	1.2987	-3.8765×10^{-3}	1.2816	1.2973	Stable
	s_5	210	2400	-4.3699×10^{-3}	1.3690	-3.8650×10^{-3}	1.3136	1.3469	Stable
	s_6	300	2400	-1.4052×10^{-2}	2.1559	-3.1258×10^{-3}	1.9568	1.9971	Stable
	s_7	400	2400	-1.8677×10^{-2}	2.4390	-9.1167×10^{-3}	2.2683	2.3428	Stable
	s_8	300	1800	-1.0787×10^{-3}	1.9936	-1.8210×10^{-3}	1.940	1.9918	Stable
	s_9	400	1800	-4.5784×10^{-3}	2.2382	-3.5098×10^{-3}	2.172	2.1845	Stable
	s_{10}	400	380	-9.1718×10^{-3}	1.2159	-9.7854×10^{-3}	1.1807	1.1848	Stable
Neutral curve	n_1	250	56.88	-2.3899×10^{-5}	4.0593	-9.8754×10^{-4}	3.8765	3.8985	Mode-4
	n_2	230	139.84	-7.6221×10^{-7}	2.5336	-5.465×10^{-6}	2.4211	2.4236	Mode-3
	n_3	284.91	310.94	-8.1041×10^{-4}	3.9059	-6.7893×10^{-4}	3.8654	3.8876	Mode-3
	n_4	485	360.24	-9.2627×10^{-4}	4.5421	-6.7543×10^{-4}	4.3458	1.1943, **4.4626**	Mode-3
	n_5	485	383.79	-2.5951×10^{-4}	1.2277	-4.3454×10^{-4}	1.1976	**1.1991** 2.4321 3.6532	Mode-2
	n_6	279.62	500	1.7793×10^{-4}	1.2989	1.5682×10^{-4}	1.2654	1.2753	Mode-2
	n_7	217	1800	-7.7874×10^{-4}	1.4029	6.3487×10^{-4}	1.3695	1.3754	Mode-2
	n_8	220	2250.0	9.7981×10^{-6}	1.5109	6.7854×10^{-6}	1.4783	1.4865	Mode-2
	n_9	273.74	1800	1.8821×10^{-6}	1.9211	5.4459×10^{-5}	1.8321	1.8943	Mode-2
	n_{10}	400	1668.75	-5.8248×10^{-5}	2.1865	-8.9831×10^{-4}	2.0421	2.0546	Mode-2
	n_{11}	600	1653.13	-8.5403×10^{-5}	2.3659	-7.5673×10^{-5}	2.3342	2.3565	Mode-2
Unstable	u_1	400	310.94	7.3598×10^{-2}	4.2654	5.4321×10^{-2}	3.9858	4.0923	Mode-2
	u_2	400	500	1.8767×10^{-2}	1.4009	1.8653×10^{-2}	1.3875	1.3921	Mode-3
	u_3	400	1000	2.9612×10^{-2}	1.8510	2.8783×10^{-2}	1.8401	1.8420	Mode-2
	u_4	300	1000	1.8925×10^{-2}	1.6839	1.9356×10^{-2}	1.6689	1.7013	Mode-2
	u_5	240	1800	2.9177×10^{-3}	1.6547	2.1234×10^{-3}	1.5766	1.61321	Mode-2
	u_6	540	379.69	4.3258×10^{-3}, -2.7337×10^{-2}	1.2190 4.6844	2.9458×10^{-3}	1.2004	**1.2119** **4.5844**	Mode-2

TABLE 1. Information of the selected control points. As the Fourier transform picks up more than one mode, the modes that match with the eigensolutions are in bold.

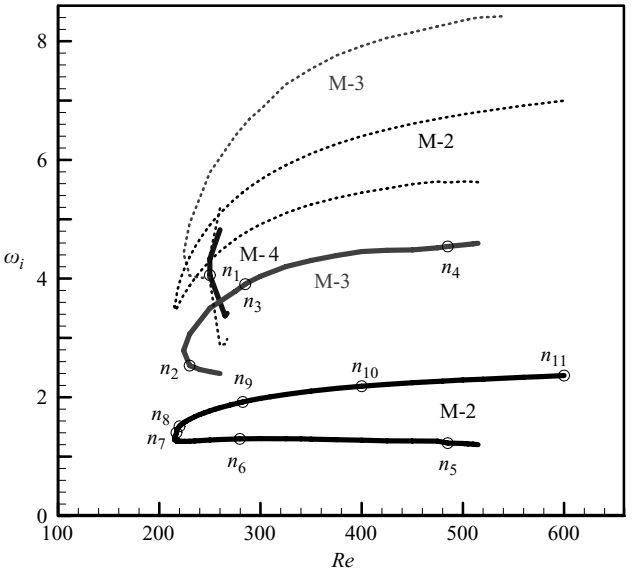

FIGURE 4. As in figure 3, but plotted in (ω_i, Re)-space. The dotted branches are the predictions by Davies & Carpenter (1997*b*), to be discussed later.

sufficiently small, i.e. the structure is very compliant. The frequencies of points n_4 and n_5 are quite different even though they are very close in the (c_λ, Re)-space. Again, this is because n_4 and n_5 represent different disturbance modes (see below).

4.5. *The eigenmodes at the neutral points*

Mode information for the neutral points can be obtained using the eigensolver. Some selected neutral points are shown in figure 5. It is immediately clear that neutral points on branch M-2 (n_5, n_8 and n_{11}) exhibit mode-2 disturbances, with two half-wavelengths along the elastic wall; the amplitude of these disturbances remains constant while that of other modes decays (figure 5*b*) (note, as the results are from the eigensolver, amplitudes shown are arbitrary, chosen to make the plots clearer). Mode-2 disturbances were those identified in earlier work (Jensen 1990, 1992; Luo & Pedley 1996). Branches M-3 (points n_2, n_3, and n_4) and M-4 (point n_1) are associated with the mode-3 and mode-4 disturbances, respectively. Although it is possible to excite all modes at any of these points, only one mode remains of constant amplitude. Even for point n_4 (on branch M-3) which is close to n_5, the mode-2 disturbance has decaying amplitude, and the mode-3 disturbance is the one that survives. For point n_5, it is the other way round since this point is located on branch M-2. This explains the marked difference in the neutral frequencies between n_4 and n_5: though their wall shapes are almost the same (see § 4.6) and the mode shapes are almost the same (figure 5), in fact, they lose stability to different modes. Note that for point n_2, mode-3 clearly dominates, while mode-2 decays rapidly. For point n_1, as it is located on branch M-4, the neutral mode is mode-4, while all other modes decay.

As two neutral branches start to merge (close to points n_4 and n_5, for example), eigenmodes from these two branches start to become similar to each other. Just before the intersection, say, at n_4, although mode-3 is the neutrally stable one, the

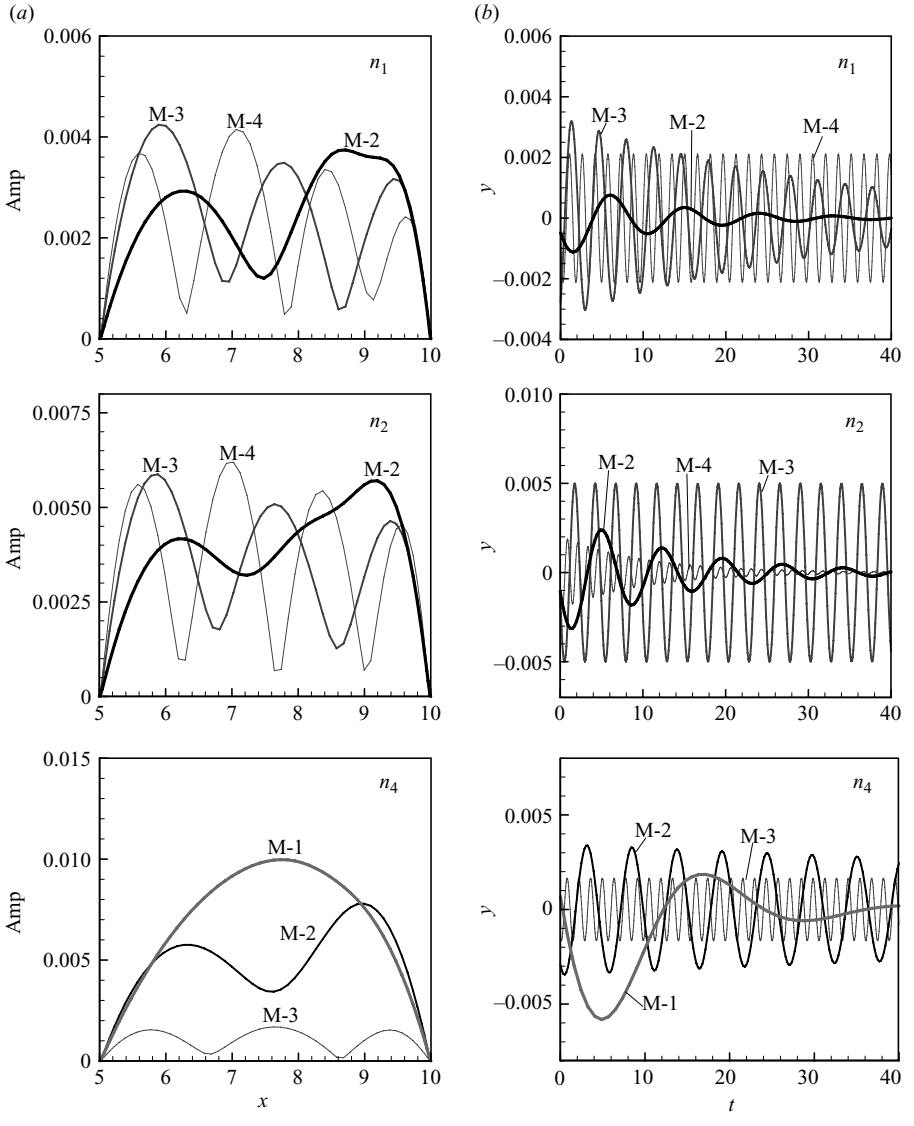

FIGURE 5. For caption see facing page.

decay rate of mode-2 becomes much slower compared to points far away from the intersection (e.g. n_3). Mode-2 then gradually takes over from mode-3 as the intersection is approached (see n_5). It is clear that when the crossing actually occurs (to locate this point exactly using our bisection approach would be excessively time-consuming and we have not done it), the two modes will both be neutrally stable, and the system will experience a double Hopf bifurcation, similar to that derived from Jensen's one-dimensional analytical model (Jensen 1990). After the intersection, operating points may lose stability to both mode-2 and mode-3 disturbances simultaneously (see the unsteady solution at point u_6, discussed below).

To understand the mode cascade further, we proceed to analyse the corresponding steady and unsteady solutions in the neighbourhood of the neutral curves, using the full numerical coupled solver.

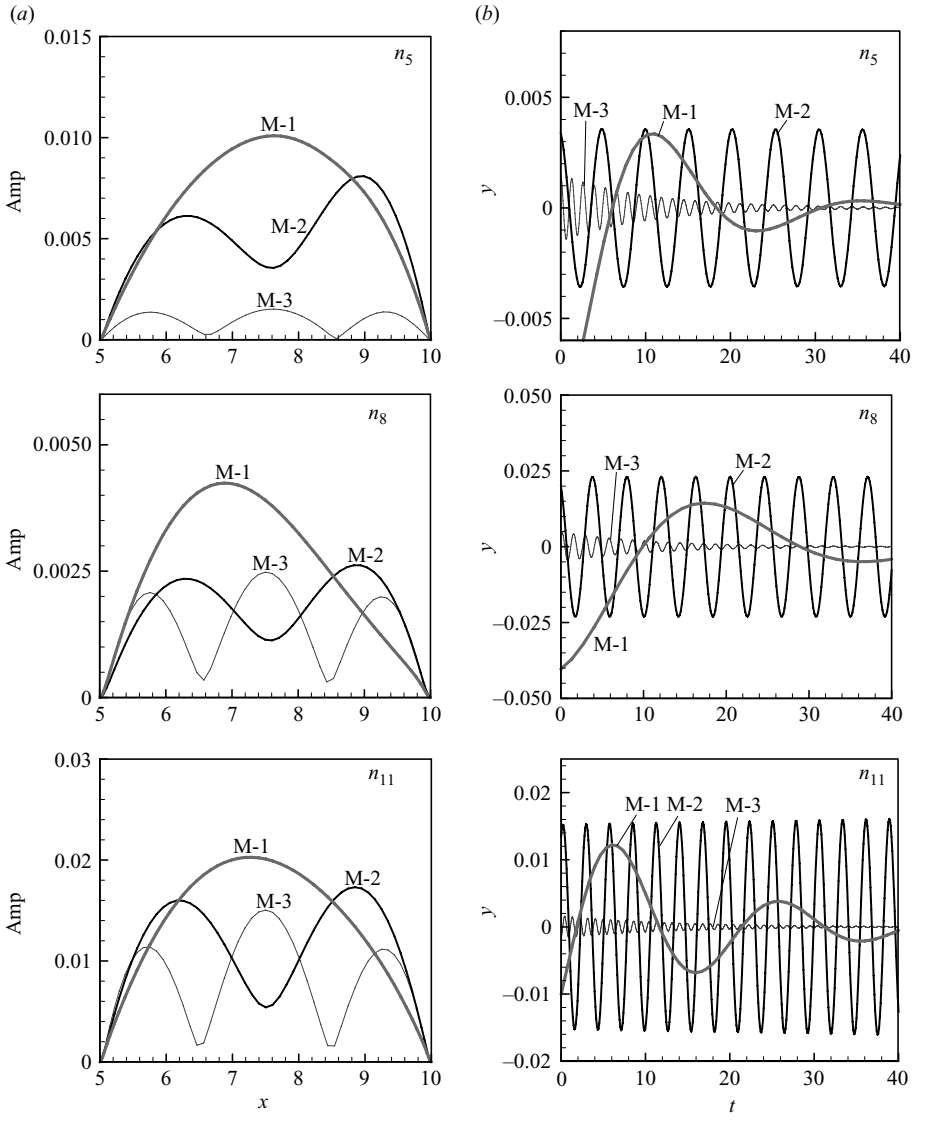

FIGURE 5. Eigenmodes of the neutral points n_1, n_2, n_4, n_5, n_8 and n_{11}. (*a*) The amplitudes of y, and (*b*) the time histories of the y displacement of a point on the beam initially at $x = 7.5$.

4.6. *The steady solutions at the neutral curves*

The steady solutions (which form the basis of the aforementioned instability analyses) are obtained using the fully coupled solver. The steady-state elastic wall shapes for some selected neutral points are shown in figure 6(*a*); these neutral points are marked on figure 3. Along the upper branch M-2, the maximum wall deformation decreases from n_{11} to n_8, while its location moves slightly downstream. Along the lower branch M-2, from n_7 to n_5, the maximum wall deformation increases, and the location hardly changes. Along branch M-3, the elastic wall has relatively large deformation and from n_4 to n_2, the wall starts to bulge out at the upstream end, the maximum deformation decreases and the maximum deformation point shifts more and more towards the downstream end of the beam. Note also that the wall shapes for n_4 and n_5 are

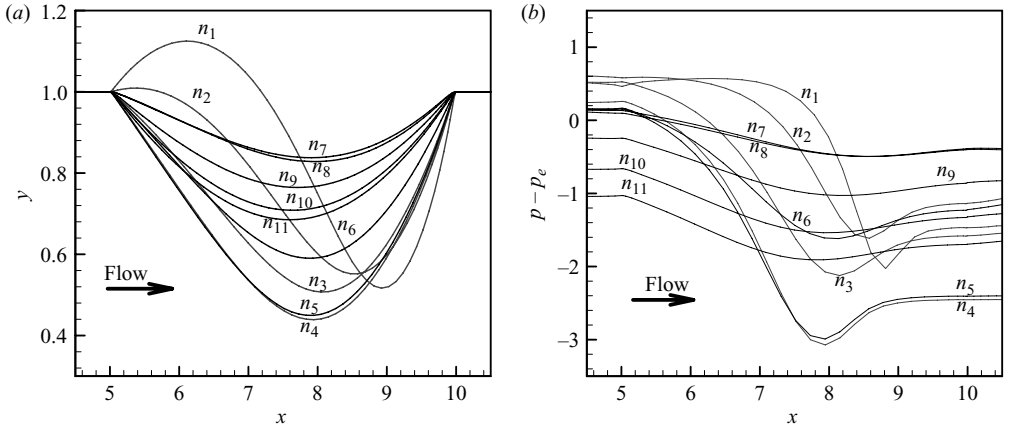

FIGURE 6. The elastic wall shapes (*a*) and the corresponding pressure (*b*) of the selected neutral points on the curve branches M-2 to M-4.

very similar. On branch M-4, the features appearing on branch M-3 are much more obvious; with upstream bulging and the maximum deformation shifting downstream (point n_1). The maximum deformation at n_1 is further downstream than at all other points and the wall slope is greater.

The corresponding steady-state pressures along the wall are plotted in figure 6(*b*). The pressure distributions are closely related to the wall shapes. Of particular interest is the difference between n_4 and n_5: though the shapes are largely similar, the pressure for n_4 is higher than n_5 at the upstream part, and lower at the downstream part. This is consistent with the slight difference between the wall shapes for these two points. Larger wall deformation is associated with a greater drop in the pressure from upstream to downstream. In addition, there are some qualitative changes in the shape of the pressure distributions. Along the upper branch M-2, the shape of the pressure distribution is markedly different from those on other branches: it is much more uniform along the elastic wall. This is not surprising as points on upper branch M-2 have much less wall deformation, therefore the pressure drop is largely caused by the friction losses associated with relatively undisturbed Poiseuille flow. However, along other branches, from n_6 to n_1, the pressure distribution has a sharp drop, with the maximum drop moving more and more downstream. This is consistent with the movement of the maximum wall displacement.

4.7. *The steady solutions at* $Re = 400$

As the results presented here are all for non-dimensional variables, care should be taken when drawing physical interpretations from these graphs. This is because both c_λ and p_e are scaled in such a way that they are proportional to Re^{-2}, see equation (1*b*). To eliminate this effect, here we will look at a set of operating points at a fixed Reynolds number, $Re = 400$.

The steady solutions at these points are shown for the wall shape (figure 7*a*), transmural pressure (figure 7*b*), wall curvature (figure 7*c*), the effective tension T_e (figure 7*d*), and the wall shear stress (figure 7*e*). Figure 7 shows clearly how, as we decrease the value of c_λ the wall deformation increases, the maximum displacement moves downstream, and the upstream end tends to bulge upwards, as indicated by the curvature changes in figure 7(*c*) (see s_{10} and u_1). In correspondence to this, the pressure drop from upstream to downstream becomes increasingly steep with an

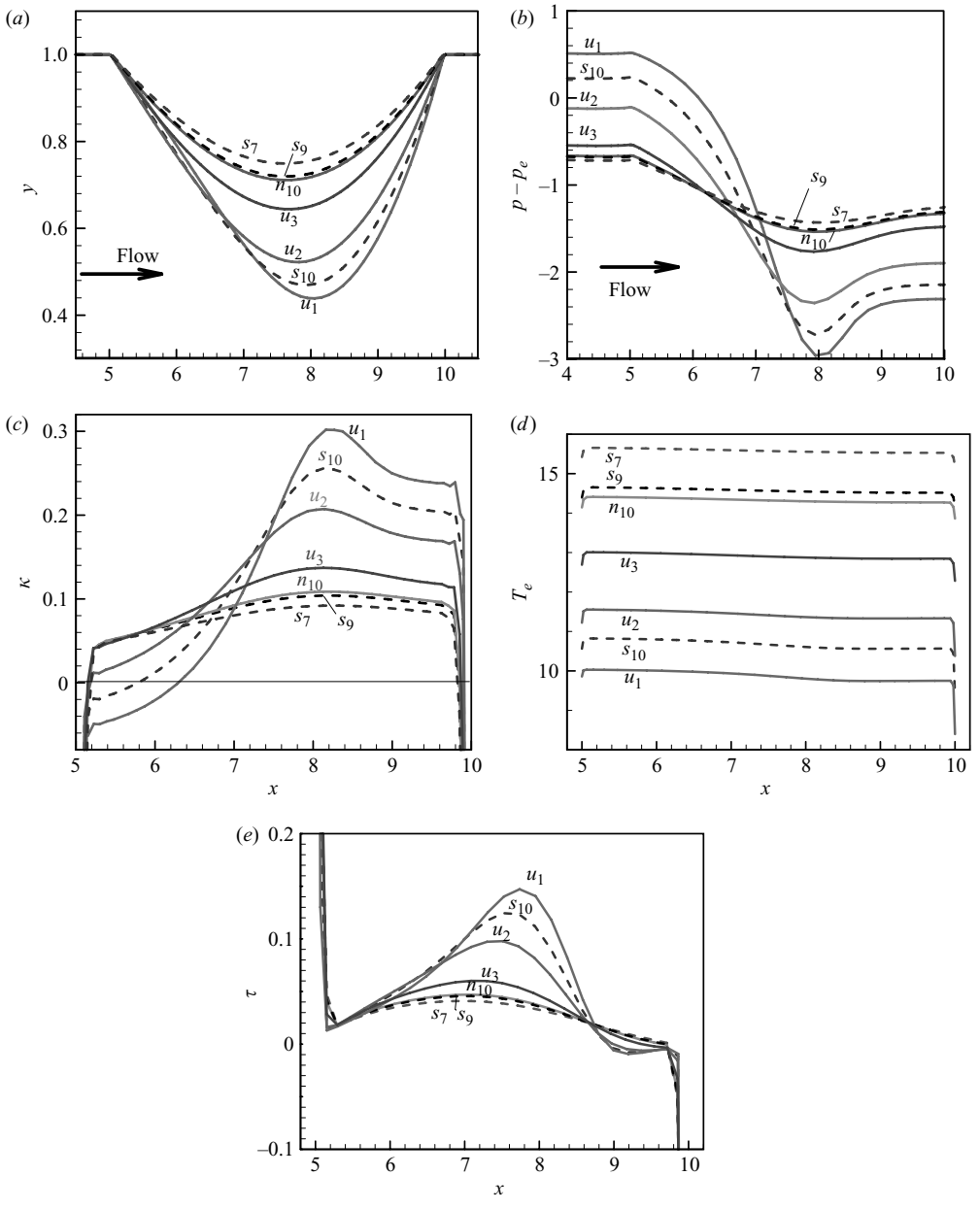

FIGURE 7. Results plotted against x for selected points at $Re = 400$ (s_7, s_9, n_{10}, u_3, u_2, s_{10}, u_1): (*a*) elastic wall shapes, (*b*) the corresponding transmural pressure distribution, (*c*) the curvature, (*d*) the effective tension, and (*e*) the wall shear stress. The steady solutions (s_7, s_9, s_{10}) are shown as dashed curves.

increasing pressure recovery downstream of the narrowest point. On the other hand, despite the increased wall deformation, the effective tension decreases as c_λ, is reduced, and it is more or less constant along the elastic wall, except towards the ends when there is a sudden drop due to the clamped boundary condition, a phenomenon which was discussed by Cai & Luo (2003). This means that the viscous shear stress is small compared to the stretch-induced tension, as is confirmed in figure 7(*e*), where the

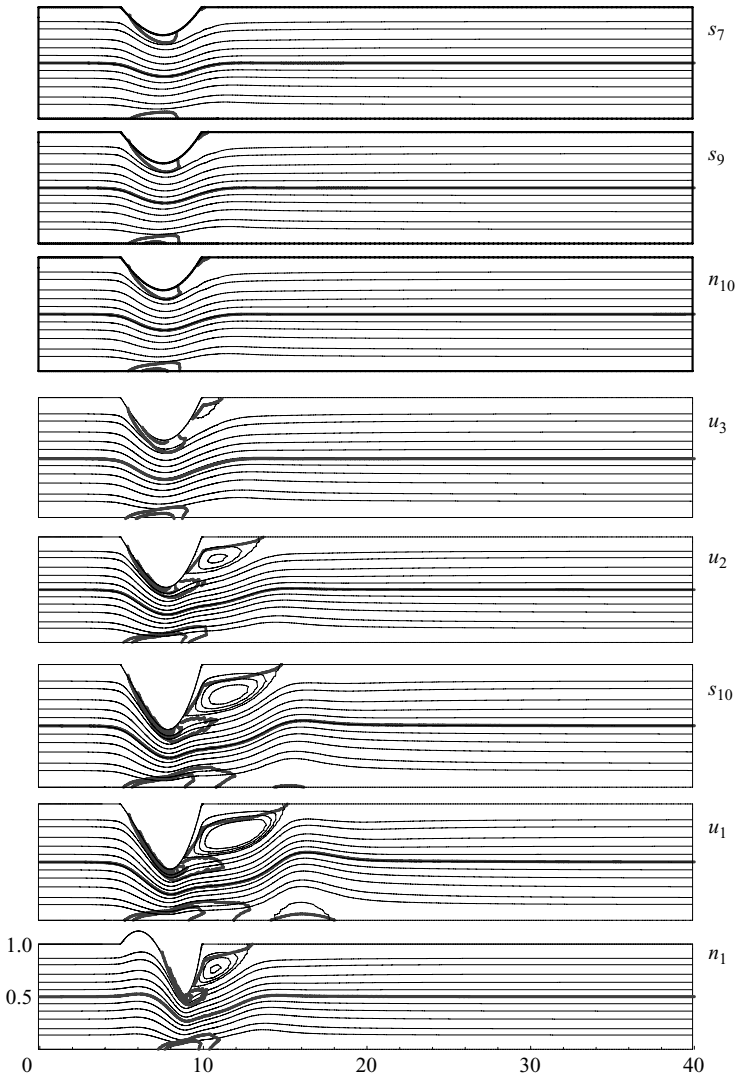

FIGURE 8. The streamlines (thin lines) and vorticity contours (thick lines) for the steady flows at selected operating points at $Re = 400$ and n_1 (see also figure 3).

order of magnitude of the wall shear stress is only about 1% of that of the tension. Although s_{10} has a more deformed wall shape and a greater pressure drop than u_3, it is a stable point whereas u_3 is not.

Steady streamline and vorticity contours for the same operating points are shown in figure 8. From these plots, it is clear that flow separation is present in all the steady solutions (though the separated flow zone is much smaller and weaker for s_7, s_9, n_{10} (not visible) and, to a lesser extent, u_3); note especially that a large recirculation occurs for s_{10}. We also note that there is almost no visible flow recirculation for n_8, but a much stronger one in n_{11} (not shown). In other words, the neutral curve is not the boundary between flows with and without flow separation. This suggests that the instability mechanism is different from that proposed for a one-dimensional model by Cancelli & Pedley (1985) and Jensen (1990), that the energy loss associated with flow

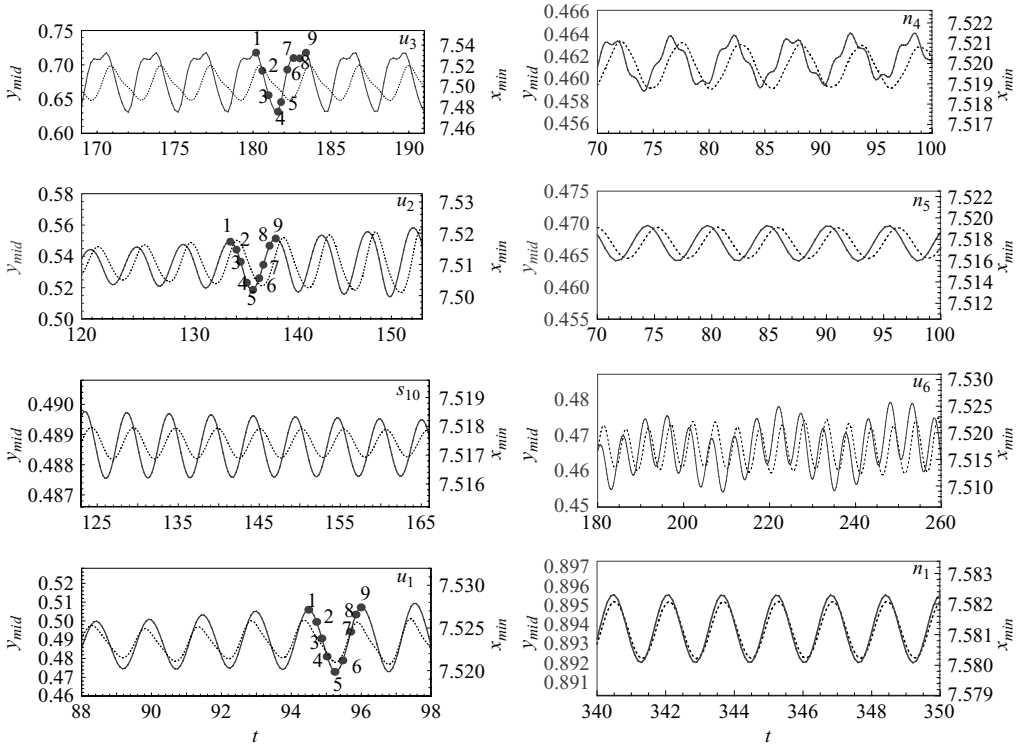

FIGURE 9. The time history of the middle point ($x = 7.5$ initially) of the beam for some operating points at $Re = 400$ (u_2, u_3, s_{10}, u_1), followed by a selection of others (n_4, n_5, u_6, n_1). The solid line is the y position and the dotted line is the x position. More detailed information for u_1, u_2 and u_3 at the selected time instants (solid circles) are shown in figures 10 to 15.

separation plays an essential role in the instability of the system. As shown by Luo & Pedley (1996, 1998), Hayashi, Hayase & Kawamura (1998), and Jensen & Heil (2003), as well as this paper, it is clear that flow separation is not a prerequisite for self-excited oscillations. The mechanism by which the system loses stability requires some energy dissipation, but this may arise in various ways, such as viscous dissipation in the boundary layer on the upstream-facing slope of the indentation, viscous dissipation on the opposite wall, flow separation, or structural damping (Hayashi *et al.* 1998), though the last is absent in the present model.

4.8. *The unsteady solutions and self-excited oscillations*

The unsteady solutions at selected operating points in the (Re, c_λ) parameter space are obtained using the fully coupled numerical solver. Oscillations are shown in figure 9 for some operating points at $Re = 400$ (u_3, u_2, s_{10}, u_1), followed by a selection of others (n_4, n_5, u_6, n_1). The curves shown are the x- and y-displacements of the material point initially at the mid-point of the elastic beam ($x = 7.5$). The solid curve is the displacement in the y-direction, and the dotted curve is the displacement in the x-direction. The results of figure 9 are plotted over a variety of time intervals, chosen to reveal the development of oscillations, before highly nonlinear behaviour arose (in the unstable cases). It will be noted that the oscillations in case s_{10} are decaying, as expected for a stable point. We see again that the oscillation patterns at points n_4 and n_5 have subtle differences here even though their corresponding steady solutions

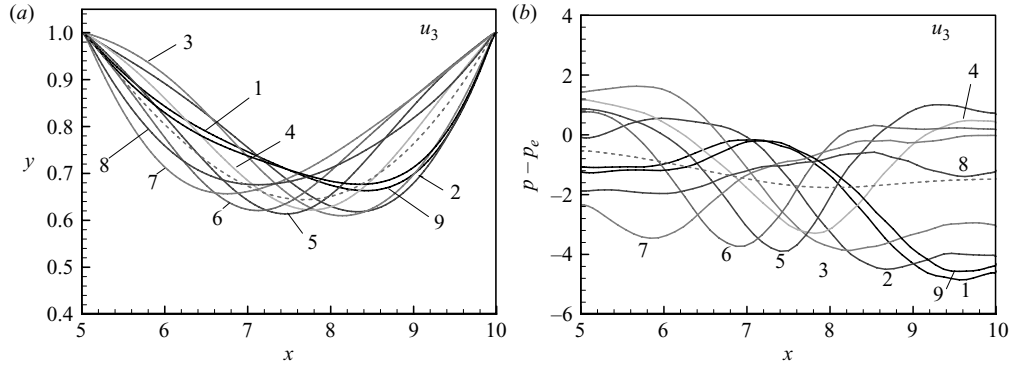

FIGURE 10. (*a*) The elastic wall shape at time instants 1–9 as indicated in figure 9, for point u_3, and (*b*) the corresponding transmural pressure distributions. The dotted curve is the corresponding steady solution.

are very similar. Although the mode-2 frequencies of these two points are similar (see table 1), it is mode-3, with a frequency almost four times higher than mode-2, that is neutrally stable for n_4.

As one goes from the neutral branch M-2 to the interior of the unstable zone (see figure 3), the oscillations tends to become more complicated with higher-frequency components being added to the neutral frequency, e.g. from u_2 to u_3. The oscillations at u_6 are especially interesting, as this is a point which is located at a region where both mode-2 and mode-3 are likely to be unstable (see figure 3). The disturbances have a frequency of about 4.6, modulated by the lower frequency of about 1.2, i.e. mode-3 modulated by mode-2 (see table 1, and discussions below).

It is also worth mentioning that the oscillations for these points are not entirely in the y-direction, which is vertical. The amplitude of oscillations in the x-direction is smaller than that in the y-direction, but is not negligible: it varies from about 10% of the y-amplitude for u_1, to 20% for n_4 and n_5, 40% for u_2, and over 50% for u_3, n_1 and u_6 in a typical period. This demonstrates that, when the deformations are large, the assumption of vertical wall movement as made in earlier studies (e.g. Luo & Pedley 1996) should be used with caution. We may also note the phase difference between the x- and y-oscillations. For some points, these appear to be more or less in phase (u_1 and n_1), for others, there is a significant phase lag (e.g. n_4, n_5 and u_3). This is also observed in the computed eigenmodes (not plotted).

The unsteady wall shapes and the transmural pressure distributions for operating points u_1, u_2, and u_3 at nine different time instants (as specified in figure 9) are shown in figures 10, 12 and 14. The instantaneous streamlines and the corresponding vortex contours are also shown in figures 11, 13 and 15. These figures show that when the system is unstable to mode-2 perturbations, the upstream and downstream end of the elastic wall is moving up and down alternately, generating a vorticity wave downstream, similar to those obtained with the membrane model (Luo & Pedley 1996). As vorticity is closely related to energy dissipation in the system, these results also show that most energy is dissipated from boundary layers on the walls, sometimes on the upstream slope of the indentation, sometimes on the downstream slope, and sometimes on the opposite wall.

The unsteady simulations from the fully coupled solver seem to support the results from the eigensolver. In order to make quantitative comparisons between the unsteady results with those of the eigensolver, we must estimate the growth rate and the

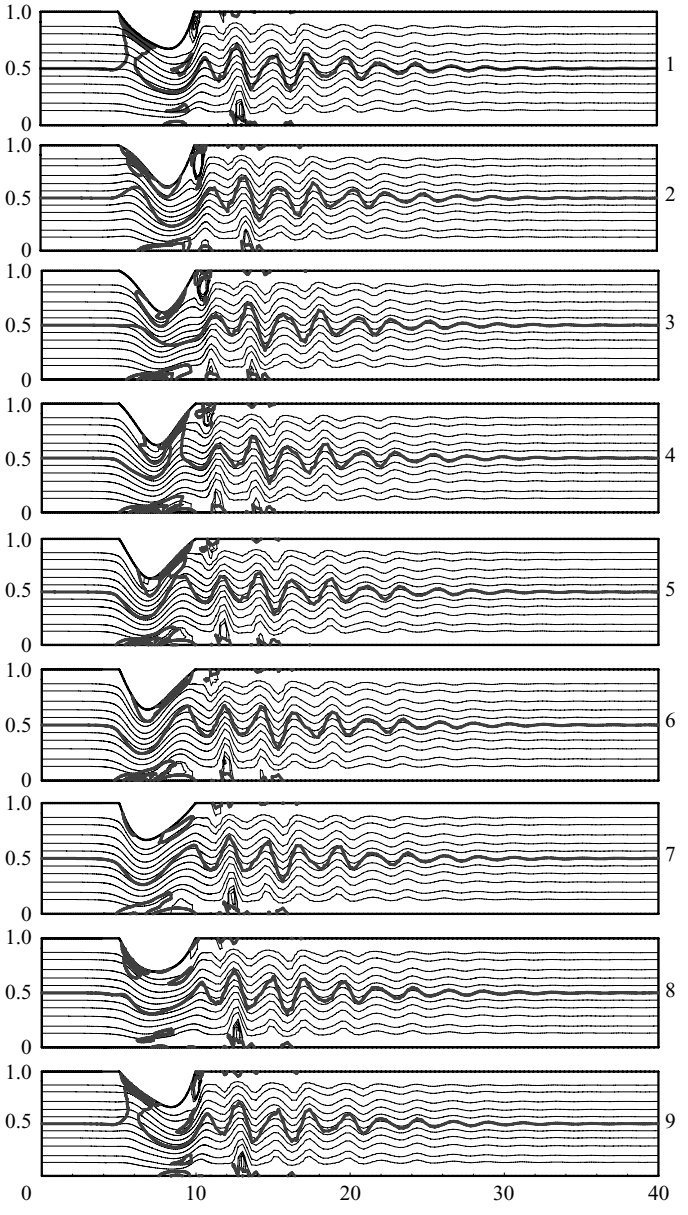

FIGURE 11. The instantaneous streamlines (thin lines) and vorticity contours (thick lines) at different time instants as indicated in figure 9, for operating point u_3. These contours are plotted equal-spaced between -0.03 to 1.03 for streamlines, and -50 to 50 for the vorticity contours.

corresponding frequency from the unsteady oscillations. Here both the Levenberg–Marquardt algorithm (Press *et al.* 2002) and the Fourier transform are used for this purpose. The Levenberg–Marquardt algorithm can estimate the growth rate as well as the frequency from the full simulations; it is only suitable for a perfectly periodic waveform (i.e. consisting of one mode only). The Fourier transform is able to extract frequencies for unsteady oscillations consisting of different modes, but is not able to estimate the growth/decay rates of these modes. Using both methods, we can estimate

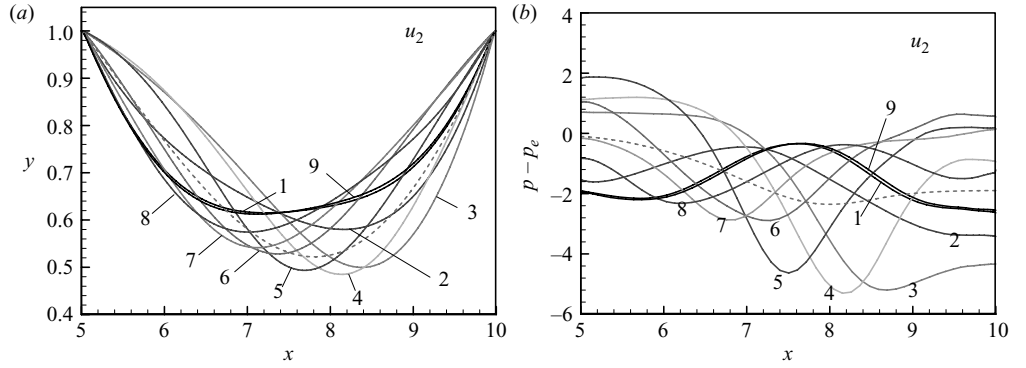

FIGURE 12. As figure 10, but for point u_2.

the frequency and growth rate of the unsteady oscillations in the y-direction, and these are compared with those from the eigensolver in table 1. When there is more than one mode from the Fourier transform, the mode which matches that of the eigensolver is shown in bold. The agreement is very good for all operating points selected, with the maximum difference in frequency predicted by the eigensolver and the unsteady simulations to be around 5%. In fact, results from the Fourier transform are also slightly different to those from Levenberg–Marquardt. They both estimate the frequency from the unsteady simulations, but the Fourier transform should be more accurate in this case as the oscillations are not perfectly periodic in a single mode. The difference in growth rates is somewhat greater. This is partly because of the limitation of the Levenberg–Marquardt scheme, which is only good for single mode oscillations, but partly because the growth rate from the eigensolver is for the whole beam structure oscillating in the dominating mode, which may not be precisely the same as the oscillations in the y-direction (or the x-direction) alone used for Levenberg–Marquardt estimation. Indeed, the self-excited oscillations in the x- and y-directions can be quite different, as shown in figure 9.

4.9. *Physical explanation for the cascade structure of stabilities*

We now offer a physical interpretation of our findings. First, consider (5) for zero wall inertia. The normal component of external force on the beam ($\sigma - p_e$, essentially the transmural pressure $p - p_e$) is balanced by (a) bending (the first r.h.s. term in (5)), and (b) the tension due to stretching (the third r.h.s. term). The second r.h.s. term in (5) is zero since $T = 0$. The tension component is the main force in the main section of the beam, while the bending component contributes significantly at the two ends.

Equation (4) shows that the viscous shear stress τ_n is responsible for longitudinal variation in stretch, λ', plus a negligible contribution from bending (first r.h.s. term). However, as we have seen (figure 7e), the variation in λ with x is very small compared with the average stretch (i.e. the magnitude of τ_n is much smaller than the average value of T_e), in the steady cases. This remains true in all the unsteady cases considered.

Thus the dominant force balance of the beam (in (5)) can be expressed as:

$$\kappa = \frac{p - p_e}{T_e}, \tag{12}$$

which essentially is a membrane equation with the variable effective tension (proportional to the unknown wall stretch $\lambda - 1$) replacing the constant tension commonly used for membrane models. As the effective tension is almost constant

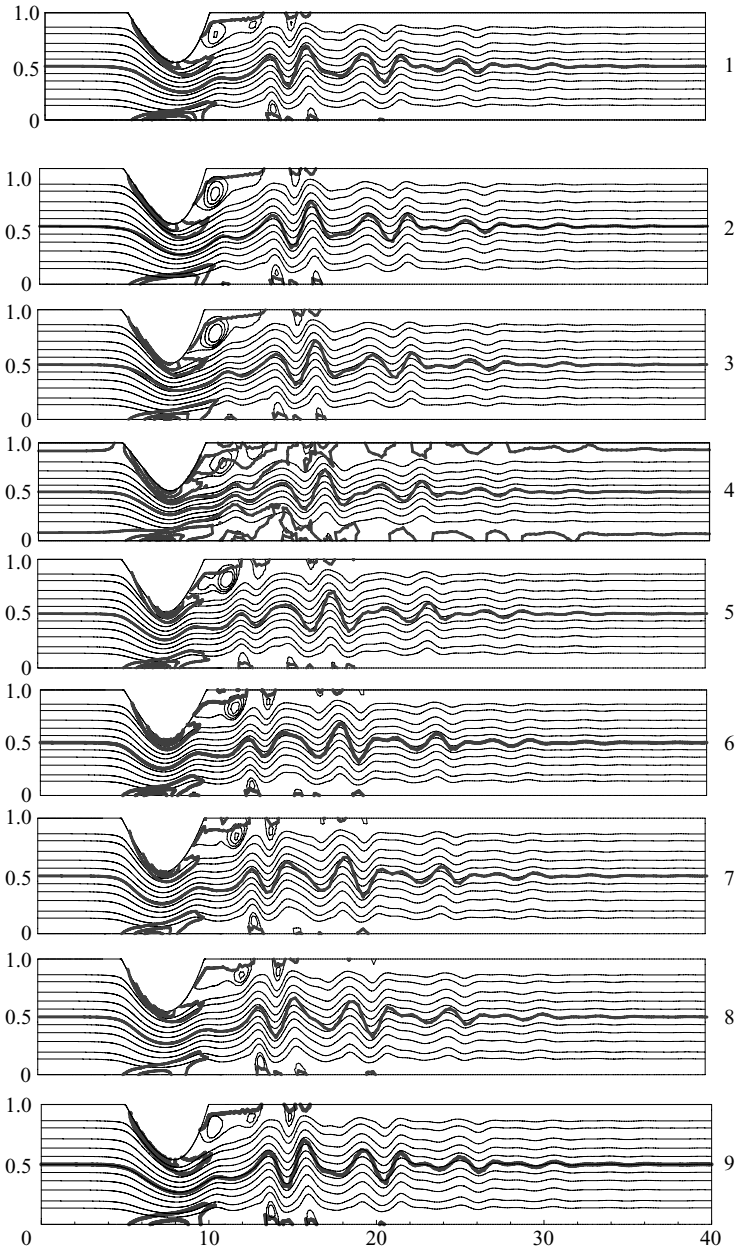

FIGURE 13. As figure 11, but for operating point u_2.

along x (see figure 7d), (12) tells us that the transmural pressure is the main force responsible for the wall curvature. In other words, although the transmural pressure in steady flows is in equilibrium with elastic forces, it can affect the stability of the system through its interaction with the wall configuration (curvature) and the flow configuration, especially flow separation. In the following, therefore, we will discuss the cascade structure in terms mainly of the transmural pressure, $p - p_e$, at various operating points around the neutral curve in figure 3, and of the occurrence of flow separation.

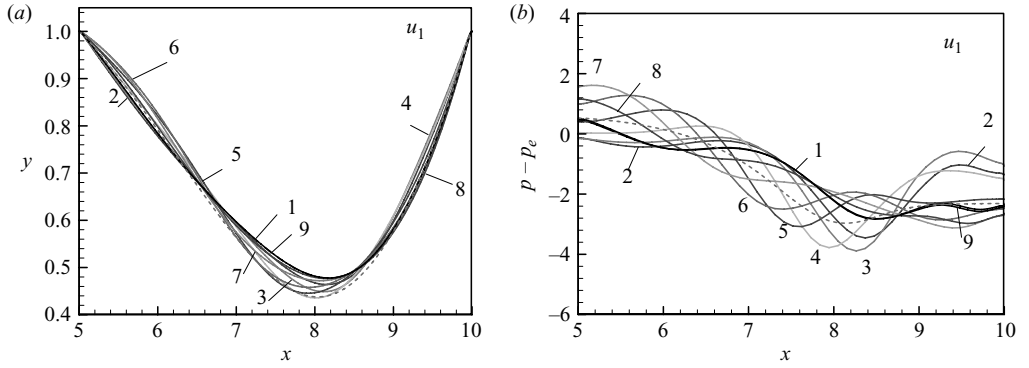

FIGURE 14. As figure 10, but for point u_1.

It is found that the system is stable for all values of wall stiffness when Re is less than 200 for the parameters investigated (figure 3). For the given external pressure ($=1.95$), the deformation is then small, the transmural pressure is more or less uniform along the elastic wall and viscosity is strong enough to damp out all disturbances.

For $Re > 200$, when inertial effects become more important, the system exhibits a cascade of linear instabilities as the wall stiffness is reduced for a fixed Reynolds number. For a very stiff wall, the beam is almost rigid and the transmural pressure is almost constant along the wall. For a given external pressure, the most likely disturbance to make it unstable is the mode-1 type, in which the whole wall would move in and out in phase. This is what Jensen & Heil (2003) predicted in their asymptotic analysis.

As c_λ is reduced, the wall deformation increases, which causes the distribution of the transmural pressure to change, with lower transmural pressure at the downstream end and greater transmural pressure at the upstream end: see operating points s_7 and s_9 in figures 3 and 7. As the effective tension is more or less uniform, this pressure distribution causes the curvature of the wall to change, see (12) and figure 7(b, c). This configuration militates against mode-1 wall perturbations; in other words, such a change in the configuration raises the critical load for mode-1, in the same way as introducing a deflection in the middle of a column supported at the two ends and subject to lateral forces delays buckling (Timoshenko & Gere 1963). So even if such instabilities had developed, they would tend to be stabilized as c_λ is reduced and the mode-1 neutral curve would come back on itself like the mode-2 and mode-3 neutral branches (a feature which is not predicted by Jensen & Heil's model as they considered only the limit of high tension).

However, as the wall becomes less stiff, this type of configuration is vulnerable to mode-2 disturbances, because the mode-2 pressure distribution tends to push the upstream half of the beam out and the downstream half in, relative to the steady state, see operating points n_{10} and u_3 in figure 7. The standard explanation for collapsible tube oscillations is the following (Pedley 1980, chap. 6). The wall displacement is enhanced by the Bernoulli effect: As the channel becomes more constricted at the downstream end, so the flow accelerates, by conservation of mass, and the pressure decreases further, enhancing the constriction. However, as the constriction becomes narrower, viscous resistance will rise in its vicinity, either through viscous dissipation in attached boundary layers, or through flow separation, requiring a bigger pressure

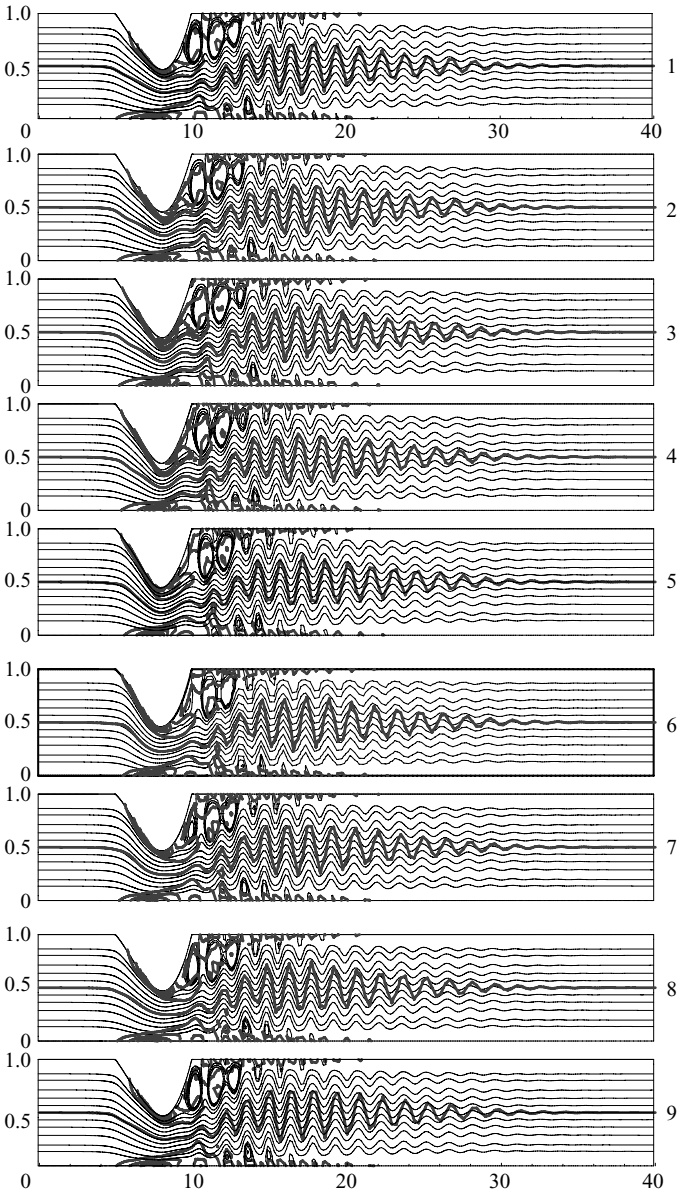

FIGURE 15. As figure 11, but for operating point u_1.

drop to maintain the flow rate. Thus upstream pressure will rise, tending to make the upstream half of the elastic section bulge out further, and eventually forcing open the constriction again. This has been recognized for many years as one of the main mechanisms for collapsible tube oscillations, and it is clearly associated with mode-2 disturbances. Thus, the system becomes unstable to mode-2 perturbations as c_λ is reduced (and crosses the upper branch M-2).

Let us consider the sequence of events in more detail for operating point u_3, with reference to figures 9, 10 and 11. This operating point is one for which the (unstable) steady state is almost unseparated, i.e. there is no visible flow separation, but a

nearly zero yet negative streamfunction value is detected at the downstream corner (figure 8). So we may start the oscillatory sequence by considering time point 8 in figure 9 (u_3), where the flow (near the beam) is similar to the steady flow (though the indentation is smaller), essentially inviscid apart from the boundary layer on the upstream slope of the indentation, with little pressure loss downstream. Then the peak indentation moves downstream, and the flow separation points moves back towards the narrowest point, with considerable pressure drop (time 9). Bernoulli's theorem operates upstream and the indentation moves rapidly inwards (times 2, 3, 4) as outlined in the preceding paragraph. However, the flow responds immediately by bending round the indentation, abolishing the separation there, with high dissipation both on the downstream slope and on the opposite wall, although separation begins there too. The attached flow on the downstream slope is associated with high-pressure recovery but, perhaps surprisingly, no immediate reseparation at the corner (time 5). The motion of the wall and the displacement of the inviscid but rotational core flow are closely coupled – as is to be expected since this is the site of generation of the downstream vorticity wave (Pedley & Stephanoff 1985). The alternation of downstream high-pressure recovery while the flow is attached and high pressure drop when it is separated, coupled with the Bernoulli effect upstream, is consistent with the observed mode-2 oscillation.

For even lower wall stiffness (operating points u_2, s_{10} and u_1) the wall is softer, the steady wall deformation increases, and the maximum deformation moves further downstream. There is a large separated-flow region in the steady flow, which is associated with some pressure recovery (figures 7 and 8). During the oscillation at point u_2, the separated flow region is elongated and split into two, this vortex shedding temporally weakens the recirculation and the flow remains attached for a long distance round the indentation (figures 9, 12 and 13, times 6, 7, 8); as for point u_3, this appears to dominate, leading to a mode-2 oscillation. However, for lower wall stiffness, and a larger indentation, the separation zone adjacent to the wall is more persistent which damps down the mode-2 oscillation and, at point s_{10}, it disappears altogether. It is replaced, at point u_1, by a mode-3 oscillation which is of smaller amplitude (figures 9, 14 and 15), and the wall motion is predominantly in the y-direction. Thus, the flow separation of the maximum indentation can act as a source either of instability at higher effective tension (e.g. point n_{10}), or of stability at lower tension (point s_{10}); we believe that the latter has not been noted previously. We also note that the steady configuration at point u_1 is the first in this sequence to show a negative curvature ('bulging') in the upstream part of the beam. The corresponding pressure distribution makes the system more vulnerable to mode-3 perturbations in which the middle part is out of phase with the two ends. The system becomes unstable again, and crosses the upper part of branch M-3, in figure 3.

Similarly, the mode-4 instability can be explained by the pressure curve for n_1 in figure 6(b), in addition to the bulging down and up at the downstream end as for mode-3 points, the pressure for n_1 is first down at the upstream corner, but is immediately pushed upwards by the flow owing to the highly compliant nature of the wall, giving the pressure distribution an extra bend. This type of distribution favours mode-4 perturbations. However, this instability is seen only for a small range of Reynolds numbers, and the flow and wall interactions soon become very complicated with competing modes as Re is increased.

We may speculate that this structure could continue in an indefinite cascade, with higher modes appearing as the beam wall stiffness is further reduced (to a material and geometric limit).

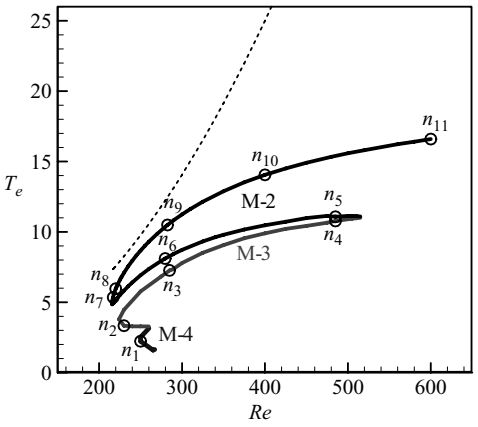

FIGURE 16. The neutral stability curve in the (*Re*, *Te*)-space for $p_e = 1.95$. Note the narrow 'tongue' found by Luo & Cai (2004) is the result of a space between the mode-2 and mode-3 branches M-2 and M-3. The dotted curve is the mode-1 instability predicted by Jensen & Heil (2003).

5. Discussion

5.1. *Further remarks on numerical accuracy*

It is indeed very difficult to perform the eigenvalue computation, as mentioned in § 3.3, especially for the higher modes, because the higher the modes, the harder it is to achieve converged results using our numerical methods. We have chosen to present results only for mode number up to mode-4 even though higher modes were captured, because we could not trust the numerical accuracy even with the finest mesh available on our computers. The best we could do was to refine the mesh at several stages, and repeatedly compare the results. We are satisfied that, at least for the results we have presented, there is no significant change in their magnitude with the grid size, and certainly no surprises in their nature (e.g. as to which mode they represent). In addition, we have run unsteady simulations, which solve a different set of equations, and the results between the two approaches agree well, thus adding further credibility to the eigenvalue results.

5.2. *Further remarks on effective tension*

The neutral curve in figure 3 can also be shown in the effective tension–*Re* space, see figure 16. In fact, in this space the neutral curve is very similar to that predicted by Luo & Cai (2004) using a *non-zero* initial tension (and a constant c_λ), even though the original neutral curves were obtained in different parameter spaces: the (*Re*, *T*)-space (Luo & Cai 2004), and (*Re*, c_λ)-space (figure 3). This suggests that the effective tension is a robust measure to compare results of different models of membranes and beams, with or without initial tension. More importantly, the stability tongue in the (*Re*, T_e)-space is almost the same as that found by Luo & Cai (2004) with a non-zero initial tension (Luo *et al.* 2007).

However, what is revealed in this study is that we now know that the tongue zone is simply the space between branches M-2 and M-3, i.e. between mode-2 and mode-3 disturbances. There is another smaller 'tongue' between the mode-3 and mode-4 branches, M-3 and M-4. Luo & Cai (2004) reported only mode-2 instabilities in their tongue zone. The reasons for this are partly due to the small differences in basic flow using the non-zero initial tension (see Luo *et al.* 2007), and partly due to a finer mesh

being used here for the eigensolver. Any inaccuracies in the original approach by Luo & Cai (2004) could make it difficult to distinguish mode-3 from mode-2 neutral instabilities, especially near branch M-3 where the absolute growth/decay rates for the two modes can be very small (see figure 5 and table 1). For the same reason, it is difficult to use the full simulations alone (for which a finer mesh was used) to identify the exact growth rates near these points, since an infinite time would be required to determine the growth rate at the neutral points. Needless to say, at large times, nonlinear effects may also come into play and the full simulations may not serve as a reliable way to identify the linear instabilities at their onset.

5.3. *Comparison with experiments*

It is found that when Re is less than 200, the system is stable. This is similar to what has been found in experimental studies of collapsible tube flows (e.g. $Re < 260$ was found to be stable by Bertram & Elliott 2001). Although there are some essential geometric differences between two-dimensional channels and three-dimensional tubes, the basic physical explanation of the instabilities may be similar for both. It is important here to realize that the mechanical properties of the elastic wall (i.e. different values of c_λ), play a significant role in the stability of the system. However, as is shown here, for a relatively thin wall (i.e. small c_κ), the role of c_λ can essentially be replaced by the effective tension. If we accept that varying the tension is equivalent to varying the length of the elastic segment (as predicted by one-dimensional theories, see Jensen 1990; Luo & Pedley 1995), then all the features discovered here could, in principle, be identified in experiments with tubes of different lengths, while keeping c_λ the same, which is much easier than changing c_λ, the mechanical property of the wall. In fact, Bertram *et al.* (1990) mapped instabilities for flow through tubes of differing length, and discovered coexistence of many modes of oscillations in the system. They also found that the frequencies increase systematically with flow rate, and the predominant effect of tube length is to predispose the system to a particular mode of oscillation. The minimum recorded frequencies are found to be higher in a shorter tube than in a longer one. Qualitatively, all these are in agreement with our observations (see figures 4 and 16) – as long as we can say that a longer tube can be compared to our case for lower tension, and a shorter one for higher tension (though this comparison is a strict one only in the one-dimensional model, see Luo & Pedley 1995). For lower tension, our cascade structure shows that more modes will become unstable, whereas for higher tension, only mode-2 is found to be unstable. However, more detailed comparison is not possible as the parameter range, and the three-dimensional nature of the experiments, are different from our case.

5.4. *Comparison with Jensen's one-dimensional model*

The mode-2 unstable behaviour predicted here agrees with the earlier observations on membrane models with large wall deformation (Jensen 1990, 1992; Luo & Pedley 1996, 1998, 2000). In fact, Jensen (1990) predicted all three modes, mode-2 to mode-4, in his one-dimensional model. It is thus interesting to compare our results qualitatively with his findings, which are very similar to ours, although Jensen's model is over-simplified in many respects. Like us, he did not find any unstable mode-1. Quantitative comparison with Jensen's results is not possible, since they are given in the flow-rate and downstream- transmural-pressure space, whereas in our model, the closest comparison we can make is the neutral curve in the (Re, EA)-space (see figure 17). However, note that Re is equivalent to Q (for fixed viscosity, diameter and fluid density), and EA is proportional to c_λ ($EA = \rho D U_0^2 c_\lambda = 10^{-7} Re^2 c_\lambda$). Note too that, from (5) for steady flows or when $\rho_m = 0$ (as is the case here), an increase in the

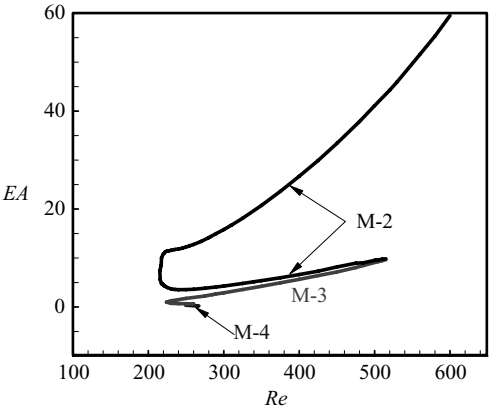

FIGURE 17. The neutral curves in the (Re, EA)-space, to be compared with Jensen's neutral curves in his one-dimensional model (Jensen 1990, figure 5).

transmural pressure at the downstream end can be provided by increasing c_λ given that $T = 0$, and c_κ is very small). Thus, it is reasonable to expect that the effect of increasing EA in our model is similar to that of increasing the downstream transmural pressure in Jensen's model. (Jensen's transmural pressure was scaled with the bending stiffness of the tube. As this bending is in the third dimension, we may treat this as independent of c_λ, at least for lower mode disturbances.) In fact, the mode-2 neutral branch in figure 17 is strikingly similar to Jensen's mode-2 neutral curve (Jensen 1990, figure 5). Although the mode-3 and 4 neutral branches in our case are different from his predictions, this may be partly because his one-dimensional model is less accurate for higher modes, but more probably because, in the higher modes, the essential differences between a three-dimensional tube and a two-dimensional channel become more significant. What is interesting in Jensen's results is that he too found that mode-2 and mode-3 neutral curves can intersect to form a double Hopf bifurcation. In addition, he predicted the ratio of the frequencies of the mode-3 and mode-2 oscillations to be just under 4, which is similar to the value found here (see table 1). Moreover, the steady solution at the mode intersection is the same, as we have found here.

5.5. *Comparison with Davies & Carpenter's linear model*

It may be informative to compare our results with earlier work addressing the relative effects of bending stiffness and membrane tension in flow-induced instability of a compliant channel with walls that are initially planar, not deformed as in our case. The work of Davies & Carpenter (1997*b*) suggests that the important structural properties which determine the system stability are tension and bending stiffness (the spring element in their model is absent here) for a massless wall. Using our non-dimensional variables, their theory (see (34) in Davies & Carpenter 1997*b*) predicted that oscillations will occur with neutral frequency

$$f = \frac{n(T + 9k^2 c_\kappa - 3/5)}{Lr}, \tag{13}$$

where $r = \sqrt{2T + 18k^2 c_\kappa - 1/5}$, T is the initial tension, k is the wavenumber (hence $n = k\pi/L$ is the mode number), L is the length of the elastic wall, and c_κ is as defined here. Note that c_λ does not appear since the membrane tension is supposed to be large enough not to change during small-amplitude oscillations. To compare our

results with theirs we must again employ the effective tension concept, and compute the frequencies from (13) using the effective tension (11), and other parameters. These are shown as dotted curves in figure 4. Their model predicts neutral curves with similar qualitative features to ours – with a double mode-2 neutral curve, and mode-3 above it, although quantitatively the frequencies they calculated are much higher than predicted here.

The qualitative similarity between the frequency curves predicted by Davies & Carpenter (1997*b*) and ours is not surprising, because the frequency in their model (13) is related to the (effective) tension and we calculated the effective tension using (11) from the steady solutions at points already predicted to lie on the neutral stability curve. Nevertheless, the good agreement implies that the mechanism of the instability may be similar in the two models and that the effective tension is a good indicator of the system behaviour.

5.6. *Comparison with Jensen & Heil's two-dimensional model*

Jensen & Heil (2003) predicted how the period and growth rate of their mode-1 self-excited oscillations change with the Reynolds number. The frequency in their paper is almost constant as Re increases, but it increases with tension. On the other hand, the growth rate increases with Re, though only for lower tensions does it become positive for Re as low as 400 (see Jensen & Heil 2003, figure 9). These findings can be compared with ours in figure 2. We also find that the growth rate and frequency increase only slightly with Re for $Re > 300$, as Jensen & Heil (2003) predicted (apart from the mode-3 ($c_\lambda = 310$) curve, which demonstrated a much greater dependency on Re). Also the frequency increases with effective tension. However, the self-excited oscillations discussed in this paper differ significantly from those reported by Jensen & Heil (2003). The most important difference is that all the instabilities of this paper are excited in modes 2–4 (i.e. the fundamental mode has two to four half-wavelength disturbances along the elastic beam), whereas they found only mode-1 disturbances. We may further note that Jensen & Heil (2003), using an energy scaling argument, predicted that the oscillation frequency should be proportional to $T^{1/2}$. This is different from the prediction (13), by Davies & Carpenter (1997*b*). However, the two models start to agree with each other when T is large enough to overcome the bending stiffness and the constant terms in (13).

Using Jensen & Heil's theory, the mode-1 neutral curve in the (Re, T_e)-space can be estimated using

$$Re \approx r_{c0}^2 T_e^{1/2}, \tag{14}$$

where r_{c0} is the critical scaled Reynolds number from which the neutral stable oscillation bifurcates subcritically. This is plotted as a dotted curve in figure 16 (where r_{c0} is estimated to be about 4 for our parameters). Clearly, around this curve, our model is stable for all modes, including mode-1. Note that Jensen & Heil (2003) predicted mode-1 instability in this regime, but the oscillations were reproduced numerically only when the upstream pressure was fixed, not the upstream flow rate as here. This is because their model predicts instability only when the downstream rigid segment is longer than the upstream one; thus prescribing the upstream flow rate (equivalent to a very large upstream length) is the stablest possible state for this mode (Jensen & Heil 2003). The other reason that we have not found mode-1 oscillations here could be that our external pressure, $p_e = 1.95$, is lower than the external pressure assumed in their model (order one), which is approximately $p_e = 5$ using our scaling. This is because we scale the pressure with channel height, and

they scale it with the (elastic) channel length which is 5 times the channel height here.

5.7. *Further remarks on the cascade structure*

The cascade structure discovered here is highly sensitive to changes in the Reynolds number, and seems to exist only for low values of critical Reynolds numbers. The structure changes when Re is higher than 540 because there the mode-2 and mode-3 branches intersect. After this point, the system can become unstable owing to at least two different instability modes, which will be coupled nonlinearly when the amplitude is not infinitesimal and the whole system becomes more complex. The self-excited oscillation at point u_6 clearly shows the influence of two competing modes, mode-2 and mode-3.

A further parallel can be drawn with the work of Guneratne & Pedley (2006). They performed a large-Reynolds-number asymptotic analysis of the steady two-dimensional problem for cases in which the transmural pressure was small enough, or the (constant) wall tension large enough, for the wall displacement to remain small. For very small p_e, they found an infinite sequence of solution branches in (p_e, T)-space which intersect the p_e-axis at eigenvalues T_n, say, where $T_1 > T_2 > T_3 > \cdots > 0$. The nth corresponding steady eigenfunction consists of n half-wavelengths, like mode-n disturbances in this paper. Most of the eigensolutions are no doubt unstable (this has not yet been analysed), giving rise to mode-n oscillations as T is reduced below T_n, in a manner not unlike figure 16.

In earlier one-dimensional models (Luo & Pedley 1995; Jensen & Heil 2003), the length of the elastic wall was scaled to be inversely proportional to the square root of tension; it would therefore be expected that the cascade structure could exist for a beam with given stiffness but different lengths. In fact, traces of such a cascade structure have already been seen in Jensen's one-dimensional model for mode-2 and higher modes (Jensen, personal communication), as well as in a study on flow over compliant walls by Davies *et al.* (2006). The latter discovered that, by fixing the tension and changing the length of the compliant surface and Re, the compliant wall loses stability to mode-1 perturbations for a range of lengths only. The implication of this finding is that a longer elastic segment can re-stabilize the system, whereas intuitively it might be thought that a longer length of elastic section would tend to destabilize it. Davies *et al.* (2006) explained this in terms of interactions of a wall instability with the fluid instability due to Tollmien–Schlichting (TS) waves which only becomes significant at a specific length scale. This is a different mechanism from the one presented here, based on changes to the pressure distribution. The TS wave explanation may well be valid in some circumstances, but the consistency of our results with those of Jensen's (1990) one-dimensional analysis, in which TS waves could not play a role, suggested that TS waves are not the only mechanism underlying the cascade structure.

In solid mechanics, it is accepted that thin structures may lose stability to different modes of perturbations as external load is increased to its critical value or the length of the structure increased. For the buckling of cylindrical shells supported at the two ends and subject to external pressure, there is a mode switching when the aspect ratio (length/radius) is changed (Timoshenko & Gere 1963; Yamaki 1984; Zhu, Luo & Ogden 2007). A 'closed loop' stability behaviour, where the unstable zone is enclosed by stable zones as deformation is increased, was also found by Haughton (1980) for the post-bifurcation behaviour of an elastic membrane.

In fact, a similar cascade structure seems to appear in a variety of related systems, often described in terms of the critical velocity (rather than wall stiffness), i.e. a system can re-stabilize for a higher velocity after losing stability at a critical velocity. This is found, for example, for a cantilevered cylinder in axial flow both in experiments and in analytical models (Paidoussis *et al.* 2002; Lopes, Paidoussis & Semler 2002; Semler *et al.* 2002, Hemon, de Langre & Schmid 2006; de Langre *et al.* 2007). These authors found that, as the flow velocity increases, the cylinder first loses stability by divergence in its first mode, which is gradually transformed to divergence of the second-mode before the system is re-stabilized. And then at a slightly higher flow velocity, the system loses stability to second-mode flutter; this is followed by third-mode flutter at a still higher velocity. A similar finding is discovered in a one-dimensional soft-palate model of snoring (Lucey & Pitman 2006; Tetlow, Lucey & Balint 2006), and for a tensioned-riser in the sea (Bearman & Huarte 2006), although in the latter, mode switching in vortex-induced vibration is related to a Strouhal frequency in the excitation, and the mechanism may be very different from what is discussed here.

Furthermore, a generic instability tongue has long been recognized as being associated with a parametric system (e.g. Grimshaw 1990; Nayfeh 1973). In theoretical work by Wu & Luo (2006) on the stability of plane Poiseuille flow, it was shown that a small imperfection (such as a wavy wall) could open up an instability tongue in the frequency and Reynolds number space. Further investigation on this system using the commercial finite-element package ADINA 8.3 also confirms the existence of a cascade structure when the wall stiffness is reduced from a critical value at a given Reynolds number (Liu, Luo & Cai 2007). All these suggest that the cascade structure presented here is a physical phenomenon. Although we have attempted to explain its physical meaning using the transmural pressure and wall configuration, it is clear that a more rigorous mathematical explanation of such a structure is desirable.

6. Conclusion

The instability of flow in a collapsible channel is studied using both the full numerical solver and the eigenvalue solver for the Navier–Stokes equations coupled to the large-deformation plane-strain elastic beam equations. It is found that the neutral stability of this system appears in a cascade structure consisting of different disturbance modes. This cascade structure shows that in the (Re, c_λ)-space, depending on the inlet boundary condition and the Reynolds number, the system may first lose stability to mode-2 perturbations as wall stiffness is lowered to a critical value. As the wall stiffness is further reduced, the system is re-stabilized before going through a sequence of higher-mode unstable zones, forming a stable 'tongue' as the result of a gap between mode-2 and mode-3 neutral branches. Extensive comparisons are made with earlier models, and differences are discussed. A physical interpretation of the cascade structure is proposed. Although this study applies only to a two-dimensional collapsible channel flow, it is expected that similar cascade structures exist in three-dimensional collapsible tube flow, and possibly other slender-body fluid–structure interaction problems.

This work is supported by the EPSRC (grant GR/M07243), the Royal Society of London (2005/R4-JP), and the Royal Academy of Engineering. Useful discussions with Professor R. W. Ogden are greatly appreciated.

REFERENCES

Barrodale, I. & Wilson, K. B. 1978 A Fortran program for solving a nonlinear equation by Muller's method. *J. Comput. Appl. Maths* **4**(2), 159–166.

Bearman, P. W. & Huarte, F. H. 2006 The hydrodynamic forces acting on long flexible circular cylinder responding to VIV. *Proc. 6th FSI, AE & FIV and N Symp. Vancouver*.

Bertram, C. D. 1982 Two modes of instability in a thick-walled collapsible tube conveying a flow. *J. Biomech.* **15**, 223–224.

Bertram, C. D. & Elliott, N. S. J. 2001 Aqueous flow limitation in uniform collapsible tubes: multiple flow-limited flow-rates at the same pressure drop and upstream transmural pressure. *Proc. ASME Bioengng Conf. 27 June–1 July, Snowbird*, vol. 50 (ed. R. D. Kamm, G. W. Schmid-Shonbein, G. A. Ateshian & M. S. Hefzy), pp. 383–384.

Bertram, C. D., Raymond, C. J. & Pedley, T. J. 1990 Mapping of instabilities for flow through collapsed tubes of differing length. *J. Fluids Struct.* **4**, 125–153.

Cai, Z. X. & Luo, X. Y. 2003 A fluid-beam model for flow in a collapsible channel. *J. Fluids Struct.* **17**, 125–146.

Cancelli, C. & Pedley, T. J. 1985 A separated-flow model for collapsible-tube oscillations. *J. Fluid Mech.* **157**, 375–404.

Carpenter, P. W. & Garrad, A. D. 1986 The hydrodynamic stability of flow over Kramer-type compliant surfaces. Part 2. Flow-induced surface instabilities. *J. Fluid Mech.* **170**, 188–232.

Davies, C. & Carpenter, P. W. 1997*a* Numerical simulation of the evolution of Tollmien–Schlichting waves over finite compliant panels. *J. Fluid Mech.* **335**, 361–392.

Davies, C. & Carpenter, P. W. 1997*b* Instabilities in a plane channel flow between compliant walls. *J. Fluid Mech.* **352**, 205–243.

Davies, C., Carpenter, P. W., Ali, R. & Lockerby, D. A. 2006 Disturbance development in boundary layers over compliant surfaces. *Laminar–Turbulent Transition, IUTAM Symp. Bangalore, India* (ed. R. Govindarajan). pp. 225–230. Springer.

Ehrenstein, U. & Rossi, M. 1993 Nonlinear Tollmien–Schlichting waves for plane Poiseuille flow with compliant walls. *Eur. J. Mech.* B/*Fluids* **12**, 789–810.

Garbow, B. S. 1978 The QZ algorithm to solve the generalized eigenvalue problem for complex matrices. *ACM Trans. Math. Software* **4**, 404–410.

Green, C. H. & Ellen, C. H. 1972 The stability of plane Poiseuille flow between flexible walls. *J. Fluid Mech.* **51**, 403–416.

Grimshaw, R. 1990 *Nonlinear Ordinary Differential Equations.* Blackwell Scientific/ Wolfe.

Grotberg, J. B. & Gavriely, N. 1989 Flutter in collapsible tubes: a theoretical model of wheezes. *J. Appl. Physiol.* **66**, 2262–2273.

Guneratne, J. C. & Pedley T. J. 2006 High-Reynolds number steady flow in a collapsible channel. *J. Fluid Mech.* **569**, 151–184.

Haughton, D. 1980 Post-bifurcation of perfect and imperfect spherical elastic membranes. *Intl J. Solid Struct.* **16**, 1123–1133.

Hayashi, S., Hayase, T. & Kawamura, H. 1998 Numerical analysis for stability and self-excited oscillation in collapsible tube flow. *Trans. ASME* K: *J. Biomech. Engng* **120**, 468–475.

Hazel, A. L. & Heil, M. 2003 Steady finite-Reynolds-number flows in three-dimensional collapsible tubes. *J. Fluid Mech.* **486**, 79–103.

Heil, M. 1997 Stokes flow in collapsible tubes: computation and experiment. *J. Fluid Mech.* **353**, 285–312.

Heil, M. & Waters, S. L. 2006 Transverse flows in a rapidly oscillating, elastic cylindrical shell. *J. Fluid Mech.* **547**, 185–214.

Hemon, P., de Langre, E. & Schmid, P. 2006 Experimental evidence of transient growth of energy before airfoil flutter. *J. Fluids Struct.* **22**, 391–400.

Jensen, O. E. 1990 Instabilities of flow in a collapsed tube. *J. Fluid Mech.* **220**, 623–659.

Jensen, O. E. 1992 Chaotic oscillations in a simple collapsible tube model. *Trans. ASME* K: *J. Biomech. Engng* **114**, 55–59.

Jensen, O. E. & Heil, M. H. 2003 High-frequency self-excited oscillations in a collapsible-channel flow. *J. Fluid Mech.* **481**, 235–268.

Jensen, O. E. & Pedley, T. J. 1989 The existence of steady flow in a collapsed tube. *J. Fluid Mech.* **206**, 339–374.

Kamm, R. D. & Pedley, T. J. 1989 Flow in collapsible tubes: a brief review. *Trans. ASME* K: *J. Biomech. Engng* **111**, 117–179.

de Langre, E., Paidoussis, M. P., Doare, O. & Modarres-Sadeghi, Y. 2007 Flutter of long flexible cylinders in axial flow. *J. Fluid Mech.*, **571**, 371–389.

Liu, H. F., Luo, X. Y. & Cai, Z. X. 2007 Sensitivity of unsteady collapsible channel flows to modelling assumptions. Comput. Struct. (submitted).

Lopes, J. L., Paidoussis, M. P. & Semler, C. 2002 Linear and nonlinear dynamics of cantilevered cylinders in axial flow. Part 2. The equations of motion. *J. Fluids Struct.* **16**, 715–737.

Lucey, A. D. & Pitman, D. M. 2006 A new method for determining the eigenmodes of finite flow-structure systems. *Proc. 6th FSI, AE & FIV and N Symp. Vancouver*.

Luo, X. Y. & Cai, Z. X. 2004 Effects of wall stiffness on the linear stability of flow in an elastic channel. *Proc. 8th Intl Conf. on Fluid Induced Vibrations*, Paris, France (ed. E. de Langre & F. Axisa), vol. 2, pp. 167–170.

Luo, X. Y. & Pedley, T. J. 1995 A numerical simulation of steady flow in a two-dimensional collapsible channel. *J. Fluids Struct.* **9**, 149–174.

Luo, X. Y. & Pedley, T. J. 1996 A numerical simulation of unsteady flow in a two-dimensional collapsible channel. *J. Fluid Mech.* **314**, 191–225.

Luo, X. Y. & Pedley, T. J. 1998 The effects of wall inertia on flow in a two-dimensional collapsible channel. *J. Fluid Mech.* **363**, 253–280.

Luo, X. Y. & Pedley, T. J. 2000 Multiple solutions and flow limitation in two-dimensional collapsible channel flows. *J. Fluid Mech.* **420**, 301–324.

Luo, X. Y., Calderhead, B., Liu, H. F. & Li, W. G. 2007 On the initial configurations of collapsible channel flow. Comput. Struct. **85**, 977–987.

Marzo, A. X. Y., Luo, X. Y. & Bertram, C. D. 2005 Three-dimensional flow through a thick walled collapsible tube. *J. Fluids Struct.* **20**, 817–835.

Matsuzaki, Y. & Fujimura, K. 1995 Reexamination of steady solutions of a collapsible channel conveying fluid, a technical brief. *Trans. ASME* K: *J. Biomech. Engng* **117**, 492–494.

Nayfeh, A. H. 1973 *Perturbation Methods.* Wiley-Interscience.

Paidoussis, M. P. 1998 *Fluid–Structure Interactions: Slender Structures and Axial Flow*, vol. 1. Elsevier.

Paidoussis, M. P. 2004 *Fluid–Structure Interactions: Slender Structures and Axial Flow*, vol. 2. Elsevier.

Paidoussis, M. P., Grinevich, E., Adamovic, D., & Semler, C. 2002 Linear and nonlinear dynamics of cantilevered cylinders in axial flow. Part 1. Physical dynamics. *J. Fluids Struct.* **16**, 691–713.

Pedley, T. J. 1980 *The Fluid Mechanics of Large Blood Vessels.* Cambridge University Press.

Pedley, T. J. & Luo, X. Y. 1998 Modelling flow and oscillations in collapsible tubes. *Theor. Comput. Fluid Dyn.* **10**, 277–294.

Pedley, T. J. & Stephanoff, K. D. 1985 Flow along a channel with a time-dependent indentation in one wall: the generation of vorticity waves. *J. Fluid Mech.* **160**, 337–367.

Press, W. H., Teukolsky, S. A., Vetterling, W. T. & Flannery, B. P. 2002 *Numerical Recipes in Fortran, the Art of Scientific Computing*, 2nd edn. Cambridge University Press.

Semler, C., Lopes, J. L., Augu, N. & Paidoussis, M. P. 2002 Linear and nonlinear dynamics of cantilevered cylinders in axial flow. Part 3. Nonlinear dynamics. *J. Fluids Struct.* **16**, 739–759.

Shapiro, A. H. 1977 Steady flow in collapsible tubes. *Trans. ASME* K: *J. Biomech. Engng* **99**, 126–147.

Tetlow, A., Lucey, A. D. & Balint, T. S. 2006 Instability of a cantilevered flexible plate in viscous channel flow driven by constant pressure drop. *Proc. 6th FSI, AE & FIV and N Symp. Vancouver*.

Timoshenko, A. P. & Gere, J. M. 1963 *Theory of Elastic Stability*, 2nd edn. McGraw–Hill.

Webster, P. M., Sawatzky, R. P., Hoffstein, V., Leblang, R., Hinchey, J. M. & Sullivan, P. A. 1985 Wall motion in expiratory flow limitation: choke and flutter. *J. Appl. Physiol.* **59**, 1304–1312.

Wu, X. S. & Luo, J. S. 2006 Influence of small imperfections on the stability of plane Poiseuille flow and the limitation of Squire's theorem. *Phys. Fluids* **18**, 044104.

Yamaki, N. 1984 *Elastic Stability of Circular Cylindrical Shells.* North-Holland.

Zhu, Y. F., Luo, X. Y. & Ogden, R. W. 2007 Asymmetric bifurcations of thick-walled circular cylindrical elastic tubes under axial loading and external pressure. *Intl J. Solids Struct.* (accepted).